

JGR Space Physics

RESEARCH ARTICLE

10.1029/2020JA028331

Key Points:

- Decreases in helium and atomic hydrogen concentration at high northern latitudes occur at the onset of mesospheric cooling events
- Small-scale GW and tidal activity drives enhanced meridional transport which extends light species decreases up to the exobase in TIME-GCM
- Accompanying decreases in O⁺ and H⁺ during middle atmospheric dynamical events have implications for the inner magnetosphere

Supporting Information:

- Supporting Information S1

Correspondence to:

M. Jones Jr.,
mcarthur.jones@nrl.navy.mil

Citation:










Jones, M. Jr., Siskind, D. E., Drob, D. P., McCormack, J. P., Emmert, J. T., Dhadly, M. S., et al. (2020). Coupling from the middle atmosphere to the exobase: Dynamical disturbance effects on light chemical species. *Journal of Geophysical Research: Space Physics*, 125, e2020JA028331. <https://doi.org/10.1029/2020JA028331>

Received 26 JUN 2020

Accepted 8 SEP 2020

Accepted article online 23 SEP 2020

Coupling From the Middle Atmosphere to the Exobase: Dynamical Disturbance Effects on Light Chemical Species

M. Jones Jr.¹, D. E. Siskind¹, D. P. Drob¹, J. P. McCormack¹, J. T. Emmert¹, M. S. Dhadly¹, H. E. Attard², M. G. Mlynczak³, P. G. Brown⁴, G. Stober⁵, A. Kozlovsky⁶, M. Lester⁷, and C. Jacobi⁸

¹Space Science Division, U.S. Naval Research Laboratory, Washington, DC, USA, ²Department of Applied Sciences, College of Arts and Sciences, Embry-Riddle Aeronautical University, Daytona Beach, FL, USA, ³NASA Langley Research Center, Hampton, VA, USA, ⁴Department of Physics and Astronomy, University of Western Ontario, London, Ontario, Canada, ⁵Institute of Applied Physics, Microwave Physics, University of Bern, Bern, Switzerland, ⁶Sodankylä Geophysical Observatory, University of Oulu, Sodankylä, Finland, ⁷Department of Physics and Astronomy, University of Leicester, Leicester, UK, ⁸Leipzig Institute for Meteorology, Universität Leipzig, Leipzig, Germany

Abstract This paper characterizes the impacts of sudden stratospheric warmings (SSWs) and mesospheric coolings (MCs) on the light species distribution (i.e., helium [He], and atomic hydrogen [H]) of the thermosphere using a combined data-modeling approach. Performing a set of numerical experiments with a general circulation model whose middle atmospheric dynamical and thermodynamical fields were constrained using a numerical weather prediction system, we simulate the effects of SSWs and MCs on light chemical species, and via comparisons with two data sets taken from the mesosphere and thermosphere, we quantify the associated variability in light species abundances and mass density. Large depletions in the observed and modeled polar H abundance in the mesosphere and lower thermosphere (MLT) occur with MC onset, as opposed to SSW onset. Depletions in all light thermospheric species at high northern latitudes extend up to the exobase in our model simulations during the January 2013 SSW/MC period, with the largest depletions simulated for the lightest species. Further, our modeling work substantiates the paradigm of increased mixing in the MLT driven by a meridional residual circulation during SSWs resulting from enhanced small-scale gravity wave and migrating semidiurnal tidal forcing; the former being the primary driver and the latter of secondary but notable importance in our model simulations. SSW/MC induced light species variability then gets projected upward into the thermosphere through molecular diffusion. Modeled light species variability during the January 2013 SSW/MC event suggests SSW/MC signatures could be present in the topside ionosphere and plasmasphere.

Plain Language Summary Sudden stratospheric warmings (SSWs) and mesospheric coolings (MCs) are episodic polar middle atmospheric (~12–80 km or ~7–50 miles altitude) dynamical weather events driven by increased wave forcing from the troposphere. These events are known to have global effects on the meteorology of the upper atmosphere (i.e., the thermosphere and ionosphere). Observational and modeling evidence presented in this study demonstrate that SSWs and MCs in the middle atmosphere act to drive changes in the chemical composition of the upper atmosphere through an intricate series of processes, set in motion by SSW/MC enhancements in lower and middle atmospheric wave forcing. Our results show that SSW/MC driven changes in particularly light species like hydrogen extend well into the transition region between Earth's atmosphere and outer space. This implies that middle atmospheric weather may have an impact on the plasma populations several Earth radii above Earth's surface (~10,000 miles or more away).

1. Introduction

In addition to solar and geomagnetic drivers, the distribution of key chemical constituents in Earth's thermosphere critically depends on the meteorology of underlying atmospheric regions, including the troposphere, stratosphere, and mesosphere. Consequently, it is now well established that dynamical disturbances of lower atmospheric origin have an important impact on the variability or space weather of

the thermosphere-ionosphere (TI) system. The effects of these disturbances on thermospheric composition can be wide ranging, covering both short/small and long/large spatiotemporal scales. For example, gravity wave and atmospheric tidal variability on seasonal time scales are known to regulate the amplitude of the TI annual and semiannual oscillation (e.g., Jones et al., 2017; Qian et al., 2009; Yue et al., 2019, and references therein), while enhanced wave forcing produced during dramatic middle atmospheric meteorological events (e.g., sudden stratospheric warmings, SSWs) has been shown to reduce thermospheric mass density (e.g., Liu et al., 2011), the atomic oxygen to molecular nitrogen ratio (O/N_2 , Pedatella et al., 2016), and subsequently the plasma density of the *F* region ionosphere (e.g., Goncharenko et al., 2018; Yue et al., 2010, and references therein). However, lower atmospheric induced variability on lighter thermospheric species that eventually become the major species in the exosphere, such as helium (He) and atomic hydrogen (H), has received far less attention, especially on time scales spanning days to weeks.

Early research efforts by Bates and Nicolet (1950), Nicolet (1961), Kockarts (1972), Hunten and Strobel (1974), Liu and Donahue (1974a), and a number of others focused on describing the large-scale distribution of both helium and hydrogen atoms in Earth's atmosphere. Atomic hydrogen in Earth's atmosphere is produced via photodissociation and associated chemical reactions with water vapor, methane, molecular hydrogen, and odd oxygen species (i.e., atomic oxygen and ozone). In the upper mesosphere and above, the chemical lifetime of H becomes comparable to or longer than dynamical time scales, implying that horizontal and vertical transport play an important role in determining its variability and spatial distribution (Brasseur & Solomon, 2005). For example, eddy and molecular diffusive processes, as well as dynamical vertical transport, strongly influence the amount of H that flows vertically from the mesopause region through the exobase (Joshi et al., 2019; Kockarts, 1972); this is the process through which Earth loses its water (Catling & Kasting, 2017; Hunten & Strobel, 1974; Liu & Donahue, 1974b).

Helium in Earth's atmosphere is constantly supplied through decay of radioactive elements in Earth's crust. Like H, the noble gas He is not gravitationally bound to Earth and escapes above the exobase (MacDonald, 1963). Also like H, the helium distribution in Earth's upper atmosphere is determined by a balance of diffusion and dynamics. For example, the well-known "winter helium bulge," which is an abundance of He in the winter hemisphere compared to the summer hemisphere (Keating & Prior, 1968), is driven by the balance of large-scale horizontal and vertical transport with molecular diffusion (Liu, Wang, et al., 2014; Reber & Hays, 1973; Sutton, 2016, and references therein). Further, early work by Kockarts (1972) also discussed the sensitivity of the winter helium concentrations to changes in eddy diffusivity down near the mesopause.

It is evident from prior research efforts that the behavior of He and H significantly depend on its flow throughout the entire atmospheric column. One particular lower and middle atmospheric phenomenon that has garnered a great deal of attention because of its global impact on the TI system is a SSW. A SSW is a significant meteorological event in the winter middle atmosphere that changes both the circulation and temperature locally, and arises due to enhanced planetary wave activity in the winter polar atmosphere. Upward propagating Rossby waves of tropospheric origin propagate into the winter polar stratosphere, where they weaken or often reverse the eastward polar jet, leading to downwelling and adiabatic heating in the stratosphere (Matsuno, 1971). The change in stratospheric circulation associated with SSWs typically leads to mesospheric coolings (MCs, Coy et al., 2005; Matsuno & Nakamura, 1979; Siskind et al., 2005, 2010) and can also lead to a secondary warming at thermospheric altitudes (Liu & Roble, 2002). Ultimately, SSWs act to dynamically couple the middle and upper atmosphere, driving significant electrodynamic and thermodynamic variability in the TI system (see reviews by Chau et al., 2012; Liu, 2016).

Observational and numerical modeling studies on the impacts of SSWs and MCs on the mass density and composition of the TI system are an active area of research (e.g., Oberheide et al., 2020; Yamazaki et al., 2015). Liu and Roble (2002) used the National Center for Atmospheric Research (NCAR) thermosphere-ionosphere-mesosphere-electrodynamics general circulation model (TIME-GCM) to study effects of a self-consistently generated SSW on the mesosphere and lower thermosphere (MLT). They found that the resulting changes in the residual meridional circulation (upward and equatorward) at high northern latitudes acted to decrease the O number density ($[O]$) at 95 km and the 5,577 Å green line emission during the peak of the SSW, consistent with earlier observations by Ismail and Cogger (1982). Miyoshi et al. (2015) found similar results for MLT O during an SSW event using the neutral atmospheric component of the Ground-to-topside Atmosphere and Ionosphere for Aeronomy (GAIA) model. Others have modeled SSW effects on the descent of thermospheric carbon monoxide (CO, McLandress et al., 2013) and odd nitrogen

species (NO_x , see for a review Funke et al., 2017) into the mesosphere. In contrast to the above studies, there has been little study of how lighter species such as He and H might respond to SSW/MC events.

This study therefore seeks to understand the impact of SSWs and MCs on thermospheric light species and mass density from the base of the MLT through to the exobase using a combined data-model approach. Specifically, we performed numerical experiments with the NCAR TIME-GCM constrained by meteorological analyses in the stratosphere and mesosphere from a high-altitude version of the Navy Global Environmental Model (NAVGE-M-HA, Eckermann et al., 2018; McCormack et al., 2017), to quantify the mechanisms responsible for driving thermospheric light species and mass density changes during SSWs/MCs. Our simulations cover the northern winter periods of 2012–2013, in which a major SSW occurred, and 2013–2014, in which a major SSW did not occur, assuming constant solar and geomagnetically quiet conditions. We validate our TIME-GCM atomic hydrogen and global thermospheric density results versus available Thermosphere Ionosphere Mesosphere Energetics Dynamics (TIMED) Sounding of the Atmosphere using Broadband Emission Radiometry (SABER) atomic hydrogen data (Mlynczak et al., 2014) in the mesopause region and orbit-derived density data (Emmert, 2009, 2015; Yamazaki et al., 2015) in the upper thermosphere, respectively. To delineate the effects of enhanced gravity wave (GW) versus migrating semidiurnal tidal (SW2) activity on thermospheric light species, additional TIME-GCM and NCAR thermosphere-ionosphere-electrodynamics general circulation model (TIE-GCM) simulations were performed in order to control the different parts of the SSW-altered wave spectrum entering the mesosphere and thermosphere. We lastly characterize the influence of middle atmospheric disturbances on O^+ and H^+ ions, the latter of which could have implications for plasma density in the inner magnetosphere. The mass loading along magnetic fields in the inner magnetosphere determines the resonant Alfvén frequency of the field lines (Menk et al., 2012).

The combined data-model results presented herein demonstrate that middle atmospheric disturbances act to reduce the light species concentration at northern high latitudes extending from the mesopause to exobase, effectively reducing their latitudinal gradients, thereby weakening, for example, the “winter helium bulge.” We also show that the timing of these northern high-latitude depletions in light species more closely align with mesospheric coolings and not sudden stratospheric warmings. Finally, our numerical experiments reveal that both enhanced GW and SW2 activity during a middle atmospheric disturbance contribute to the modeled light species and mass density depletions in the thermosphere, the relative roles of which can only be diagnosed from a hierarchy of middle and upper atmospheric models that provide the flexibility to control different parts of the upward propagating wave spectrum.

2. Models, Simulations, and Data

2.1. NCAR Thermospheric General Circulation Models

The NCAR thermospheric general circulation models (TGCMs) are hydrostatic general circulation models that self-consistently model the composition, dynamics, electrodynamics, and energetics of Earth's middle and upper atmosphere (Dickinson et al., 1984; Richmond et al., 1992; Roble & Ridley, 1994; Qian et al., 2014 and references therein). These models solve the momentum, energy, continuity, and electrodynamic equations from first principles on a regular spherical grid in longitude, latitude, and log-pressure coordinates up to the pressure level of $\sim 4.6 \times 10^{-10}$ hPa (roughly 500–700 km depending on solar cycle) or what is assumed to be at or near the exobase. The NCAR TGCMs come in two flavors, a purely thermosphere-ionosphere model, the TIE-GCM with a bottom boundary at ~ 97 km (or $\sim 5.5 \times 10^{-4}$ hPa) and a version which includes the mesosphere, the TIME-GCM with a bottom boundary near 30 km (12 hPa). In this study, we use both.

The NCAR TGCM simulations performed herein were run at a resolution of $2.5^\circ \times 2.5^\circ$ (longitude \times latitude) with four model grid points per vertical scale height. Solar irradiance values spanning the X-ray and extreme ultraviolet (EUV) regions of the solar spectrum follow the formulation presented by Solomon and Qian (2005), while far ultraviolet solar radiation is specified by Woods and Rottman (2002). These values are then scaled by the Richards et al. (1994) EUVAC model, depending on a user-specified or measured F10.7 solar radio flux value and its 81-day average to account for temporal variations in the X-ray, EUV, and FUV portions of the solar spectrum. Magnetospheric coupling with the ionosphere is parameterized using an empirical ion convection model by Heelis et al. (1982) and an auroral particle precipitation model by Roble and Ridley (1987). The strength of this magnetosphere-ionosphere high-latitude coupling is determined by

using either a user-specified hemispheric power value (after Evans, 1987) and cross-polar cap potential, or using measured 3-hourly K_p (after Emery et al., 2012).

As noted above, a key difference between the two models is that the TIME-GCM's lower boundary is in the stratosphere. Therefore, the TIME-GCM accounts for physical processes important to the stratosphere and mesosphere, including photodissociation of species like ozone, methane, and water vapor, and a gravity wave drag parameterization, as well as solves a minor species continuity equation for atomic hydrogen. The TIE-GCM does not include any of this physics since its purpose is to simulate the atmosphere above the mesopause. Specifically, subgrid-scale GWs in TIME-GCM are parameterized following a linear saturation scheme by Lindzen (1981), including molecular viscous dissipation at MLT altitudes (see additional resources including Yamashita et al., 2010; Wang et al., 2017 for more details). This GW parameterization can be turned off to separate out small-scale gravity wave effects on thermospheric composition (e.g., Jones et al., 2017; Jones, Emmert, et al., 2018).

Also of particular importance for our study is lower boundary forcing. Both TIE-GCM and TIME-GCM are typically driven at the model lower boundary by climatological zonally and diurnally averaged horizontal winds, temperatures, and geopotential heights and atmospheric tidal perturbations. However, the lower boundaries of these models can be forced by different modeled or observed data sets, and in the case of TIME-GCM even employ different techniques to constrain middle atmospheric wind and temperature fields. Methods such as flux coupling the TIME-GCM to a lower atmosphere model (e.g., Liu & Roble, 2002) or ingesting reanalysis data sets via Newton relaxation (e.g., Jones, Drob, et al., 2018; Maute et al., 2015; Wang et al., 2017) have proven useful in examining SSW effects on the TI system. We will use the latter to constrain middle atmospheric winds and temperatures for our current work.

2.2. NAVGEM-HA

To constrain the TIME-GCM middle atmospheric horizontal winds and temperature we use reanalysis data from the NAVGEM-HA (see Hogan et al., 2014; Kuhl et al., 2013, and references therein for a more detailed discussion). Middle atmospheric conditions in NAVGEM-HA are constrained by assimilation of satellite-based observations from both research and operational satellites. Specific observations and their sources are as follows: (1) temperature, ozone mixing ratio, and water vapor mixing ratio (version 4) retrievals from the Microwave Limb Sounder (MLS) on board the NASA Aura satellite (Yan et al., 2016); (2) temperature profiles from version 2.0 SABER retrievals (Rezac et al., 2015); and (3) microwave radiances from the upper atmosphere sounding channels of the Special Sensor Microwave Imager/Sounder (SSMIS) on the Defense Meteorological Satellite Program (DMSP) platforms (Swadley et al., 2008). Further details can be found in McCormack et al. (2017) and Eckermann et al. (2018). The data assimilation component of NAVGEM-HA produces global synoptic analyses of important meteorological parameters (including horizontal winds and temperature) every 6 hr (00, 06, 12, and 18 UT), which then are used to initialize short-term forecasts, ultimately producing a 3-hourly analysis/forecast product each day up to ~ 100 km. This 3-hourly cadence is advantageous for our study because it reproduces semidiurnal tides (specifically the SW2) known to intensify during SSW events.

Recently, McCormack et al. (2017) validated the NAVGEM-HA system using numerous independent ground-based meteor radar (MR) wind observations during the 2012–2013 boreal winter. In this study, NAVGEM-HA wind and temperature fields from the 2013–2014 boreal winter months will also be used to constrain middle atmospheric winds and temperatures in the TIME-GCM. Therefore, Figure 1 offers *independent* validation of NAVGEM-HA mesopause meridional winds from several different MR sites, including Sodankylä (Hocking et al., 2001; Lukianova et al., 2015), Collm (Jacobi, 2012; Stober et al., 2012), and the Canadian Meteor Orbit Radar (CMOR, Brown et al., 2008) during 7–21 January in 2013 and 2014. NAVGEM-HA meridional winds (black lines) generally reproduce MR observations (blue lines) at these three high northern latitude sites during both January 2013 and 2014, including both their day-to-day variability, as well as prominent semidiurnal fluctuations observed by the different MRs. The good agreement between NAVGEM-HA and MR winds in Figure 1 lends confidence in the meteorological analyses used to constrain TIME-GCM simulations performed as part of this work.

2.3. Constrained TIME-GCM Simulations

To investigate the effects of SSWs and MCs on the light species distribution from the mesopause through to the exobase, we conducted TIME-GCM simulations in which the stratospheric and mesospheric horizontal

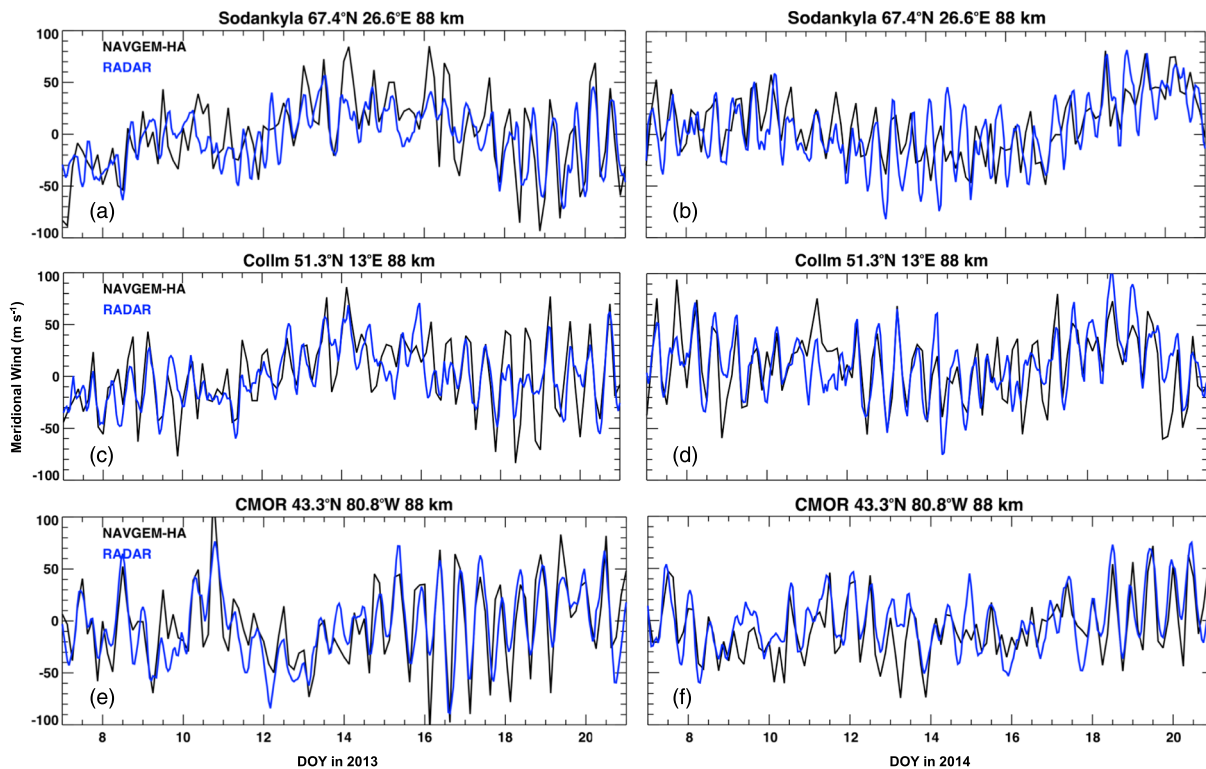


Figure 1. Time series of meridional winds from 3-hourly NAVGEM-HA analyses/forecasts (black) and from hourly meteor radar observations (blue) during 7–21 January 2013 (first column) and 2014 (second column) over Sodankylä (a and b), Collm (c and d), and CMOR site (e and f) at 88 km.

wind (u and v) and temperature (T) fields were constrained using four-dimensional tendency nudging (originally called 4-D data assimilation by Stauffer & Seaman, 1990, 1994) during the boreal winters of 2012–2013 and 2013–2014 (i.e., 1 December through 1 March). The nudging technique is described in much more detail for the interested reader in Jones, Drob, et al. (2018). Essentially, an extra momentum or energy tendency term is added to the right-hand side of the horizontal momentum and thermodynamic energy equations that is proportional to the difference between the modeled and NAVGEM-HA u , v , or T scaled by a Newtonian relaxation factor. Thus, this extra momentum or energy tendency source term acts as a correction to the TIME-GCM momentum and energy equations. Also, the nominal TIME-GCM lower boundary conditions are replaced with NAVGEM-HA analyses/forecast using a normalized vertical weighting function of unity. Above the lower boundary, this weighting factor decreases with altitude (pressure) and becomes zero at TIME-GCM log-pressure level -7 (or $\sim 5.5 \times 10^{-4}$ hPa), corresponding to the top of NAVGEM-HA fields. Above TIME-GCM log-pressure level -7 , the model is free-running (see the top panel of Figure S1 and associated equations in the supporting information for more details).

Nudged TIME-GCM simulations were run from 1 December to 1 March of both northern winter periods of interest, whereby results from 1–19 December are not shown and considered model spin-up. This was determined by a time weighting function (see the bottom panel of Figure S1 in the supporting information) that ensured gradual transition from an initial TIME-GCM simulation driven just at the model lower boundary to a nudged model state, in order to alleviate spurious artifacts. To isolate SSW and MC effects on thermospheric light species our simulations assumed constant solar and geomagnetic forcing, including daily and 81-day averaged F10.7 values of 130 sfu, a hemispheric power value of 15 GW and cross-polar cap potential drop of 30 kV, corresponding to a K_p value of 1. The 2012–2013 and 2013–2014 northern winter months were relatively active periods of geospace variability (see the observed F10.7 and K_p values in Figure S2 of the supporting information), and so eliminating the strong solar and geomagnetic influences on thermospheric light species was necessary in order to highlight middle atmospheric disturbance effects alone. Comparisons between model results using constant versus realistic and time-varying solar and geomagnetic inputs are provided in the supporting information.

Finally, unlike the work of Siskind et al. (2014) and Wang et al. (2017) the eddy diffusion coefficient (K_{zz}) in our TIME-GCM simulations is not reduced. These studies (and others) reduced model calculated K_{zz} values to account for the increased mixing caused by including realistic wave perturbations in the NCAR TGCMs. As Jones et al. (2017) and Siskind et al. (2019) demonstrated, reducing the absolute K_{zz} values in TIME-GCM mainly affects the absolute concentration of MLT and thermospheric species, not their variability. Therefore, leaving the model eddy diffusion coefficient unchanged is assumed to be negligible with respect to the relative changes in thermospheric light species due to a middle atmospheric dynamical event.

2.4. SABER H Data

To validate TIME-GCM simulated light species responses to middle atmospheric variability, we compared our modeling results with SABER atomic hydrogen measurements. SABER H has been compared with models by Qian et al. (2018) and Siskind et al. (2018), with an emphasis on seasonal and solar cycle variability. Here we look at the shorter-term variation in response to several SSW/MC events during the lifetime of SABER, including January 2006, 2009, and 2013 events, as well as January 2014, in which no SSW/MC occurred. The derivation of the SABER H abundance is based upon both the SABER ozone data and SABER measurements of the vibrationally excited hydroxyl airglow; this is discussed in depth by Mlynchak et al. (2014). Note, Mlynchak et al. (2018) have presented some updates to the H retrieval based upon new information about OH(ν) kinetics and showed that the retrieved H could be lower than the current operational SABER product. We did not use this latest data set because Mlynchak et al. (2018) remarked that the SABER ozone used in the derivation of the H atom concentration may change in the future. The ozone derived from 9.6 μm emission measurements is likely too large (see Smith et al., 2013) and is being examined by the SABER team as of this writing. Thus, our present work focuses on the change in H and is not dependent upon $\sim 35\%$ uncertainties in the absolute abundance (Mlynchak et al., 2014). A discussion of the similarities and differences between the older and current SABER H data sets in the context of the present work is offered in the supporting information (specifically Figure S3), as well as below in section 3.2.

2.5. Orbit-Derived Global Average Mass Density Data

We verify that our TIME-GCM simulations are consistent with observed upper thermospheric mass density perturbations; however, we use a different approach than for the comparisons with SABER. Rather than focus specifically on the 2012–2013 and 2013–2014 northern winter periods exclusively, we use a superposed epoch analysis to define a climatological SSW response, following the approach of Yamazaki et al. (2015). First, we start with a 1967–2013 time series of global average mass density, as a function of altitude, derived from orbit data on $\sim 5,000$ objects (Emmert, 2009, 2015). We then compute density anomalies by subtracting the output of the Global Average Mass Density Model (GAMDM), for each day. GAMDM (Emmert, 2015; Emmert & Picone, 2010) is an empirical climatology that describes the average behavior of the orbit-derived density data as a function of solar activity, geomagnetic activity, day of year, and tropospheric carbon dioxide levels; we use GAMDM version 2.1 (Emmert, 2015). Next, we collect 50-day segments of the anomalies around the 37 SSW events used in Yamazaki et al. (2015), including the 2012–2013 event studied in this paper. Finally, we average the 37 anomaly segments to produce a time profile of the estimated climatological response of global average thermospheric density to SSWs, which we compare with our TIME-GCM thermospheric densities in section 3.3.

Consideration of the climatological SSW response is appropriate because the TIME-GCM simulations discussed herein were performed assuming constant geospace variability during the 2012–2013 SSW event, when the Sun was quite active with a number of C- and M-class flares (see Figure S2 in the supporting information). The climatological SSW response in thermospheric density provides a more robust statistical picture of the true SSW-driven impact on global thermospheric mass density even during solar and geomagnetically active periods: GAMDM largely filters out the solar signatures in the data, leaving the middle atmospheric influences in which we are interested.

3. Results and Discussion

3.1. The 2012–2013 and 2013–2014 Boreal Winter Periods

In this subsection, we characterize the prevailing middle atmospheric conditions during the 2012–2013 and 2013–2014 northern winter periods, as well as define important time periods therein that we use as the basis for discerning seasonal from SSW/MC effects on light chemical constituents. Figure 2 illustrates the

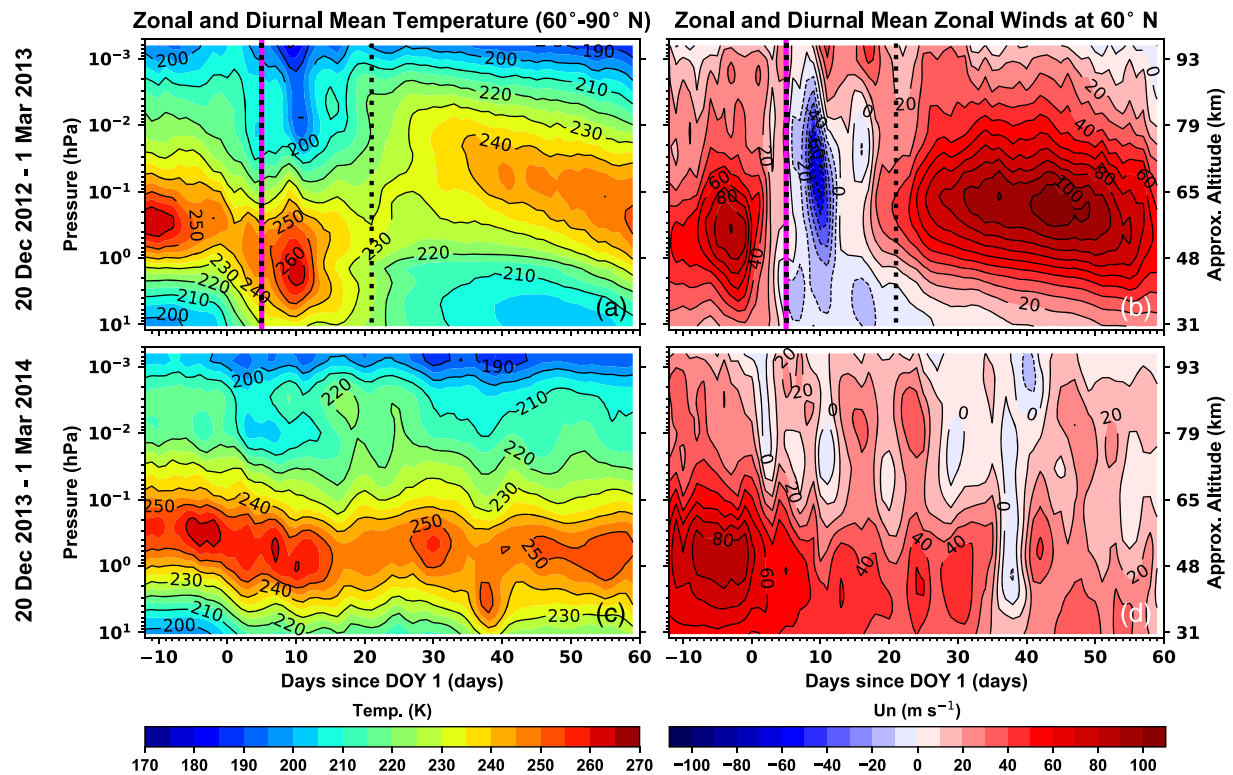


Figure 2. NAVGEM-HA zonal, diurnal, and latitudinal cosine-weighted mean temperatures between 60°N and 90°N geographic latitude (a, c) and zonal and diurnal mean zonal winds (U_n) at 60°N geographic latitude (b, d) from 20 December 2012 to 1 March 2013 (top row) and 20 December 2013 to 1 March 2014 (bottom row). Values along the abscissa represent the day of year since 1 January, with 0 being 1 January. The magenta-black hatched vertical line on 6 January 2013 denotes the onset of a strong SSW and MC event at northern high latitudes, whereas the dotted black line on 22 January 2013 marks the return to predisturbed conditions in the mesosphere. Temperature (zonal wind) contours are shown every 10 K ($\pm 10 \text{ m s}^{-1}$).

thermodynamical conditions from NAVGEM-HA analysis/forecasts during the 2012–2013 and 2013–2014 northern winter periods. Starting on 6 January 2013, polar stratospheric temperatures increased sharply by 20–30 K, with overlying mesospheric temperatures decreasing by about the same amount (Figure 2a). Associated with this increase in temperature, there is a decrease in stratospheric and mesospheric eastward winds, and in early to mid-January of 2013 zonal mean westward winds reached values of up to -60 m s^{-1} in the stratosphere and mesosphere (Figure 2b). Maute et al. (2015), Zülicke et al. (2018), and others have shown that the January 2013 SSW and MC event was the result of enhanced planetary wave 2 activity driven by a split in the polar vortex. The magenta-black hatched vertical line on 6 January 2013 signifies the onset of the SSW/MC, representing the day the zonal mean zonal winds reversed from eastward to westward at 10 hPa. The dotted black line on 22 January 2013 signals a rewarming and return to eastward winds in the mesosphere marking the beginning of the so-called “extended” phase of the SSW (see Siskind et al., 2010). Therefore, 6 January to 22 January 2013 is what we refer to as the “disturbed” time period, while the 20 December 2012 to the 5 January 2013 time frame is what we refer to as the “predisturbance” period.

It is evident by comparing Figures 2a and 2b with Figures 2c and 2d, that a major SSW and MC event occurred during early January 2013, the initial phase (i.e., 6–22 January 2013 when zonal mean westward winds and a downward displacement of the stratopause was present) of which persisted for some 15–20 days, while no such event occurred in late 2013 or early 2014. Except for some minor activity in mid-February, which does not reach the definition of an SSW, the 2013–2014 northern winter period was relatively quiet, exhibiting the typical seasonal spatiotemporal structure observed during northern winter. Important for the analysis in section 3.3, note that the comparison of 2012–2013 northern winter with the 2013–2014 northern winter is useful because it allows us to separate out seasonal effects that might have occurred over the 1-month period in question from SSW effects (like those discussed in Liu, Miyoshi, et al., 2014).

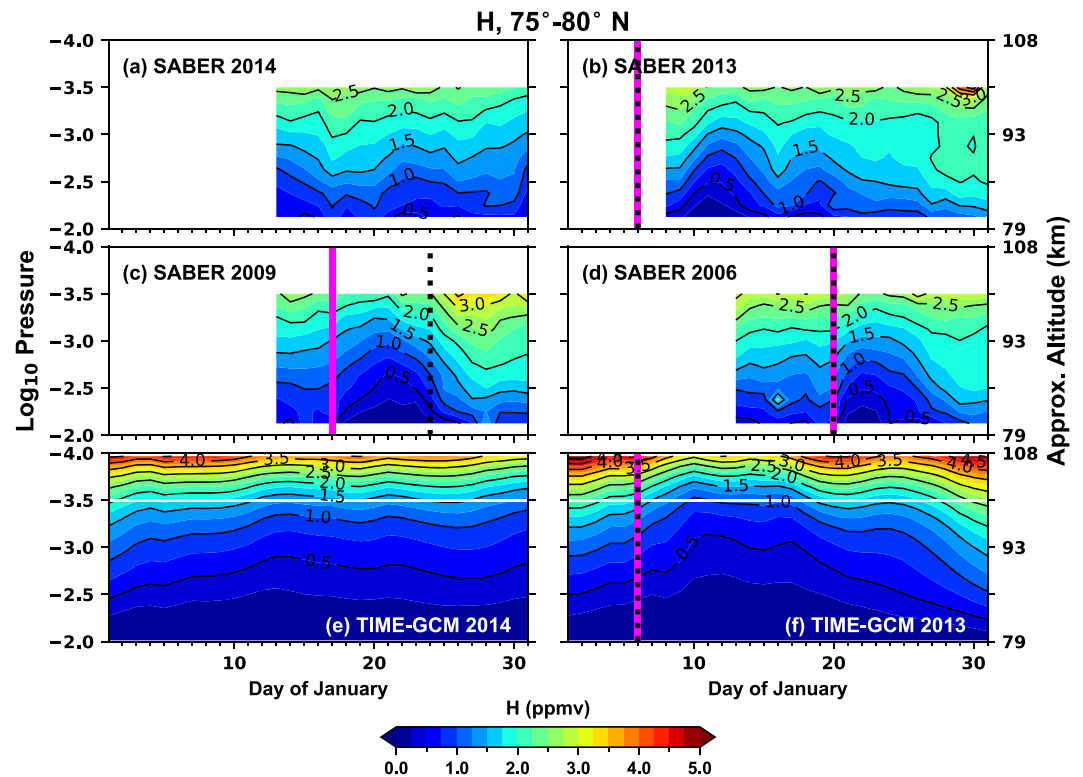


Figure 3. SABER and TIME-GCM zonal mean atomic hydrogen mixing ratio (ppmv) averaged between 75°N and 80°N during January as a function of pressure level. Shown are SABER measurements for January 2014 (a), 2013 (b), 2009 (c), 2006 (d), and TIME-GCM results for January 2014 (e) and 2013 (f). The magenta line marks the onset of a mesospheric cooling, the black dotted line denotes the onset of a sudden stratospheric warming, and where the two overlay one another marks the simultaneous onset of a SSW and MC. The white horizontal line in (e) and (f) represents the top pressure level at which SABER measures. Zonal mean H contours are shown every 0.5 ppmv.

3.2. MLT Atomic Hydrogen from SABER and TIME-GCM

First, we validate our modeling results against the SABER atomic hydrogen data set. Figure 3 shows both SABER and TIME-GCM zonal mean H as function of day of year in January and pressure for some of the recent major SSW and MC events, including 2006, 2009, and 2013. Also shown in Figures 3a and 3e are SABER and TIME-GCM zonal mean H in January 2014 when a SSW or MC did not occur. Due to the yaw maneuver required by the instruments onboard the TIMED satellite, SABER H data poleward of ~55°N are unavailable in early-to-middle January, and thus not shown in Figure 3. The solid magenta line in Figure 3 marks the onset of a mesospheric cooling, the black dotted line marks the onset of a sudden stratospheric warming, and where the two lines overlap signifies that the onset of the SSW and MC were concurrent. During the 2013 SSW/MC event, the nudged TIME-GCM reproduces the zonal mean H morphology observed by SABER. Specifically, on 8 January 2013 both SABER and TIME-GCM show a clear upward buckling in zonal mean H contours, indicating a decrease in H abundance. This is consistent with previous observations (Ismail & Cogger, 1982) and numerical experiments (Liu & Roble, 2002; Miyoshi et al., 2015) that showed decreases in O abundance during strong middle atmospheric disturbances. Consistency between observed and modeled H and O decreases at MLT altitudes indicates that they are driven by SSW/MC induced transport because both H and O have relatively long chemical lifetimes at these altitudes during polar winter. Note that SABER zonal mean H does appear to recover back to predisturbance values quicker than TIME-GCM, taking roughly 2 weeks, while TIME-GCM zonal mean H values take about 3 weeks. Figure S3 shows that the latest SABER atomic hydrogen data for the January 2013 SSW/MC event is in excellent agreement with the older SABER H data in terms of relative change. Also, the new absolute H abundances are lower, actually in better agreement with our TIME-GCM values in Figure 3f.

Figures 3c and 3d demonstrate that this decrease in atomic hydrogen associated with SSWs and MCs is robust and present for some of the other major middle atmospheric disturbances studied over the last 15

years. In January 2006, the onset of the stratospheric warming and mesospheric cooling occur simultaneously (similar to the 2013 event), whereas the mesospheric cooling led the stratospheric warming by about a week during the 2009 event. The timing of the MC versus the SSW onset for the 2009 event has been the subject of some disagreement in the literature. Using meteorological analyses from the predecessor to NAVGEM-HA, NOGAPS-ALPHA (Navy Operational Global Atmospheric Prediction System-Advanced Level Physics High-Altitude), Coy et al. (2011) identified mesospheric precursors, specifically a reversal in the winds, that preceded, by about a week, the major SSW occurring on 24 January 2009. Their results were consistent with gradient winds derived from Aura Microwave Limb Sounder observations (Manney et al., 2009), as well as meteor radar data between 80 and 100 km presented by Kurihara et al. (2010). By contrast, recent work by Zülicke et al. (2018) appears to show that temperature increases at 10 hPa (defining the SSW onset) occur concurrently with temperature decreases at 0.01 hPa on 17 January 2009. Figure 3 shows that the SABER hydrogen data agree with the earlier MC onset dates presented by Manney et al. (2009), Kurihara et al. (2010), and Coy et al. (2011). Thus, we conclude that the sharp decrease in H abundance occurs at onset of the mesospheric cooling and not the sudden stratospheric warming in 2009.

In January 2014, TIME-GCM zonal mean H is also consistent with SABER zonal mean H through mid-January, even in the absence of any middle atmospheric disturbance. Clearly, there is no sharp decrease in either the observed or modeled zonal mean H when a SSW or MC does not occur. We therefore deduce that the observed and modeled zonal mean H changes in January 2014 reflect those of typical seasonal variability. Finally, the modeled relative changes in atomic hydrogen due to a middle atmospheric disturbance, or lack thereof, are fairly constant even when including realistic geospace variability during January 2013 and 2014 (see Figure S4) within the viewing altitudes of SABER (horizontal white lines in Figure 3).

3.3. Light Species Changes From the MLT to Exobase

Global observations of neutral composition between the mesopause and exobase are sparse, and therefore we must use our TIME-GCM simulations to probe the variability in light species associated with SSWs and MCs in this “thermospheric gap” (Oberheide et al., 2011). Figure 4 shows TIME-GCM differences in O, N₂, and so-called light species He and H during and prior a SSW/MC (“disturbed-predisturbance”) in 2012–2013, as well as the seasonal changes in these species in 2013–2014. It shows a reduction in light species number densities of ~50% or more around 100 km and below. Also below 100 km, where the mass of O is about half that of the mean molecular mass of the background atmosphere, O behaves like a light species exhibiting large high-latitude reductions in our model simulations. This modeled reduction in light species in the polar regions extends well into thermosphere consistent with previous modeling and observational studies (e.g., Liu & Roble, 2002; Oberheide et al., 2020; Pedatella et al., 2016), although it becomes weaker with altitude. These weaker decreases in light species with altitude could be related to the long molecular diffusive time scales of helium and atomic hydrogen (i.e., on the order of at least a month or more at ~120 km). Still, helium and atomic hydrogen reductions of ~8% and ~17%, respectively, extend up to 500 km and to the model upper boundary.

These polar reductions in [O], [He], and [H] are mirrored by low-to-middle-latitude increases, with these increases for helium and atomic hydrogen extending through to the upper thermosphere, while low-to-middle-latitude increases in atomic oxygen are limited to below ~100 km. Note these modeled low-to-middle-latitudes increases in H abundance during a SSW and MC could be more a result of the time periods we selected for our differences, as SABER H between 30°N and 35°N does not show that large of an increase in the 2012–2013 winter (see Figure S5). However, Medvedeva et al. (2019) reported local increases in [O] from spectrometric observations between ~50°N and 55°N during the January 2013 SSW. Given these observational differences, our numerical experiments may offer some insight into the cause of such discrepancies.

Molecular nitrogen at polar latitudes exhibits the exact opposite behavior to that of the light species, with large increases (~20–60%) extending well into the upper thermosphere. The implications of N₂ enhancements for projecting light species depletions into the upper thermosphere are discussed below in section 3.4.3. Further, light species depletions and enhancements in N₂ at polar latitudes are robust as TIME-GCM simulations that include observed space weather conditions (i.e., observed daily F10.7 and 3-hourly Kp) show similar results to those with constant space weather conditions, although with larger relative changes (Figure S6).

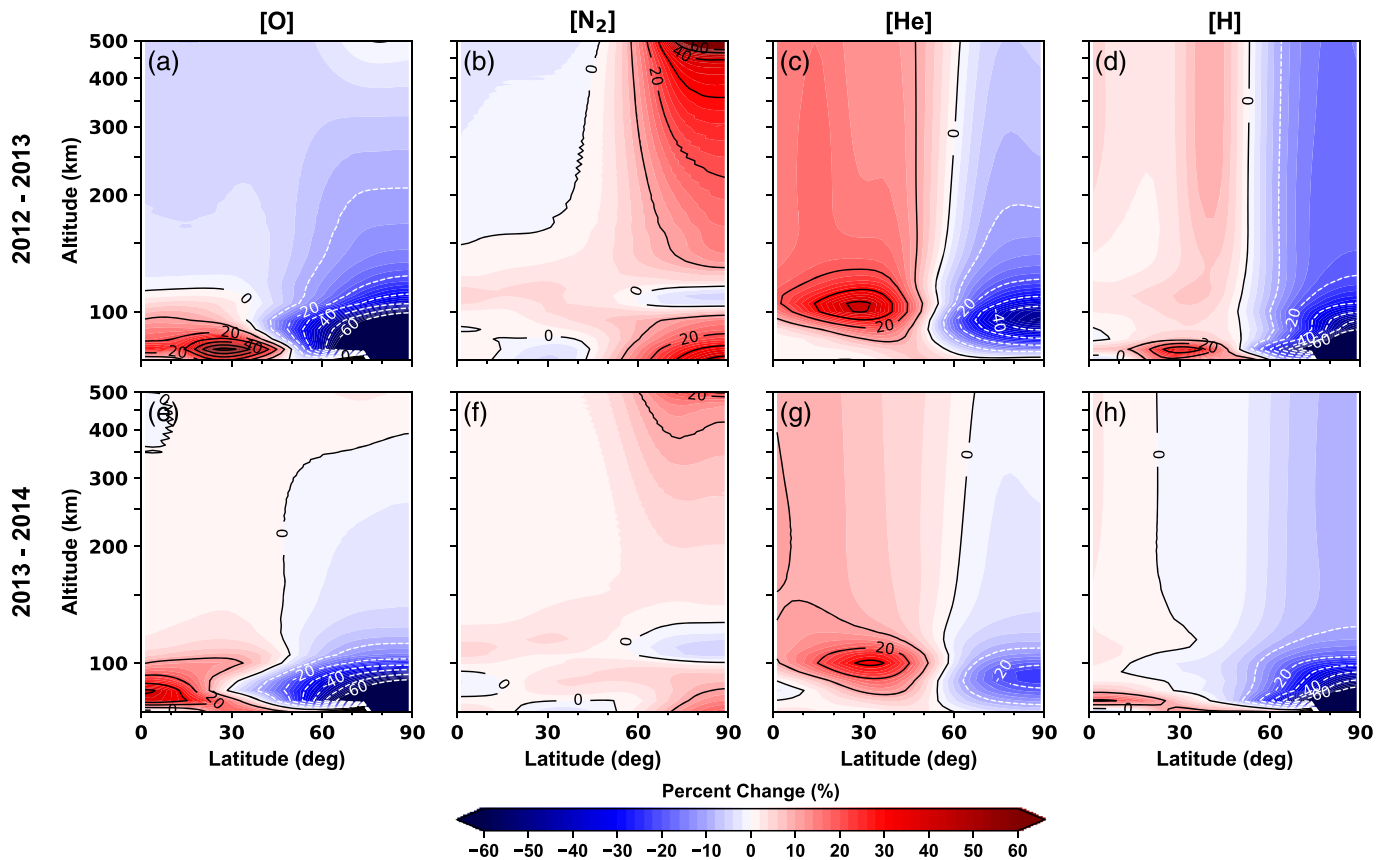


Figure 4. Percent changes in zonally averaged [O] (a and e), [N₂] (b and f), [He] (c and g), and [H], (d and h) as function of altitude in the Northern Hemisphere between the “disturbed” and “predisturbance” time periods in 2012–2013 (top row) and equivalent time periods in 2013–2014 (bottom row). Differences are contoured every $\pm 10\%$.

During the 2013–2014 winter, when no SSW or MC occurred, modeled light species depletions in the polar region are much weaker above 100 km. For example, [H] depletions at 500 km are about half of those calculated for during the 2012–2013 winter, demonstrating that sudden stratospheric warmings and mesospheric coolings act to amplify the “climatological” seasonal reduction in light thermospheric species (compare top row with bottom row of Figure 4). The same is true for N₂ but in the opposite sense, that is high-latitude N₂ increases are larger as a result of SSWs and MCs. Also, there is at least $\sim 5\%$ decrease in [O] above about 200 km globally in 2012–2013 that is nonexistent the following year. This global [O] decrease suggests a reduction in the total thermospheric mass density above 200 km, where O becomes the dominant thermospheric constituent.

Figure 5 offers model validation of global averaged mass density in the upper thermosphere against the climatological SSW response presented by Yamazaki et al. (2015). Modeled percent changes in globally averaged mass density at 400 km (Figure 5b) and 550 km (Figure 5a) from TIME-GCM simulations covering the 2012–2013 and 2013–2014 winters relative to 1 January are shown in the red and blue curves, respectively, while the averaged orbit-derived density data response of 37 different SSWs from Yamazaki et al. (2015) is shown in green. Note, the orbit-derived superposed epoch analysis curve extends from 20 days prior to 30 days after the minimum in the zonal mean zonal wind at 70° N and 1 hPa (i.e., $t = 0$). This occurred on 9–10 January 2013, so that even though the modeled global average mass density anomalies are calculated from 1 January (or time = -9 in Figure 5, where $\Delta\rho = 0$), the time = 0 are approximately equivalent between TIME-GCM results and the superposed epoch analysis performed by Yamazaki et al. (2015).

TIME-GCM global average mass density reductions for the January 2013 SSW/MC event reproduce the average orbit-derived mass density anomalies. Both reach a minimum of 5–7% at 400 and 550 km, with the superposed epoch analysis values recovering more quickly than the modeled values. Differences in modeled versus observed recovery times can be attributed to the strength and duration of the January 2013 event

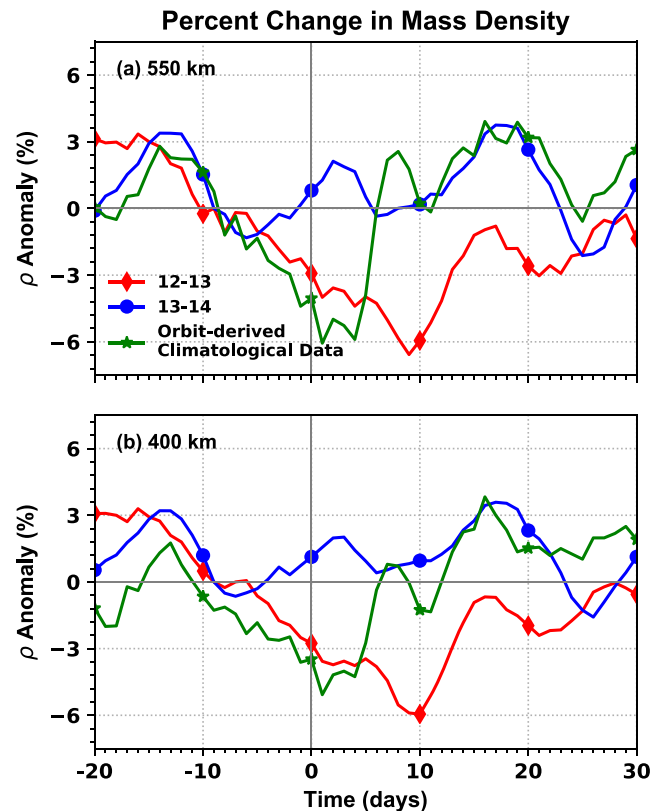


Figure 5. Percent changes in globally averaged mass density relative to 1 January at 400 (b) and 550 km (a) during the 2012–2013 (red diamonds) and 2013–2014 winters (blue circles) from TIME-GCM, and a superposed epoch analysis spanning 1967–2013 using orbit-derived density data (green stars).

compared to the climatological response of 37 different SSWs. Since the effects of the 2013 event persisted for many weeks following the initial SSW/MC, modeled thermospheric mass density depletions also persist for a month or more. Conversely, the 2013–2014 winter global average mass density anomalies in TIME-GCM never get below -1% and are generally greater than 0% throughout much of December and January. This indicates that dynamical middle atmospheric events act to reduce upper thermospheric mass density. At these altitudes, O is the major thermospheric species, suggesting that modeled O depletions are consistent with observations. The results in Figure 5 coupled with the modeled thermospheric species behavior in Figure 4 demonstrates that the TIME-GCM is capable of producing the observed variability in composition from the mesopause through to the exobase during SSWs and MCs.

3.4. Dynamical Changes in the MLT Driving Thermospheric Light Species Changes

Several studies have investigated the response of MLT and upper thermospheric composition to SSWs (e.g., Oberheide et al., 2020; Pedatella et al., 2016; Yamazaki et al., 2015). From these studies, three general mechanisms responsible for changes in thermospheric composition have been suggested. Specifically, two mechanisms propose changes in the meridional circulation (e.g., Laskar et al., 2019; Oberheide et al., 2020) due to enhanced small-scale gravity wave (Yiğit & Medvedev, 2016) and/or migrating semidiurnal tidal forcing (Pedatella et al., 2016), while the third invokes changes in eddy diffusive mixing and molecular diffusion via temperature changes (Yamazaki et al., 2015). These different processes and their relative contributions to the light species changes shown in Figures 3 and 4 are examined below. We exclude eddy diffusive mixing from our diagnosis because the SSW/MC driven changes in K_{zz} in our 2012–2013 simulations compared to K_{zz} changes in 2013–2014 were small. This could be the result of the GW parameterization in TIME-GCM and its potential shortcomings, including the uncertainty of the small-scale GW spectrum at the model lower boundary (Yamashita et al., 2010). For example, high-resolution models like those described in Yiğit and Medvedev (2012) and Zülicke and Becker (2013) designed to resolve small-scale GWs, and therefore more rigorously calculate K_{zz} , would be better suited than TIME-GCM for such an analysis.

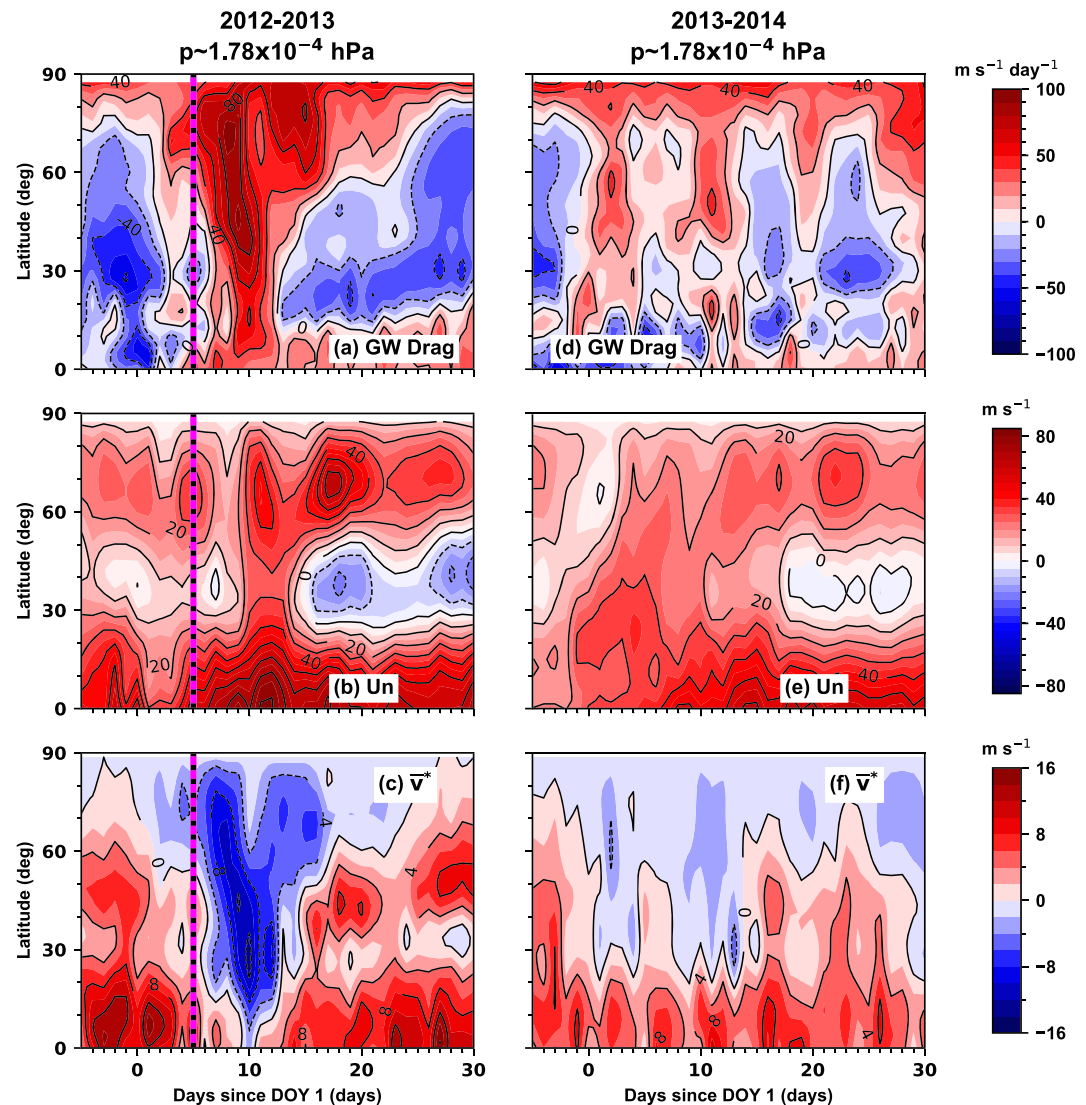


Figure 6. Time series of modeled zonally and diurnally averaged gravity wave drag (GW Drag, a and d), zonal winds (Un, b and e), and the meridional residual circulation (\bar{v}^*) in the Northern Hemisphere during the 2012–2013 (first column) and 2013–2014 (second column) winters at $\sim 1.78 \times 10^{-4}$ hPa or ~ 103 km. The magenta-black hatched vertical line on 6 January 2013 denotes SSW and MC onset. GW Drag, Un, and \bar{v}^* are contoured every ± 20 $\text{m s}^{-1} \text{ day}^{-1}$, ± 10 m s^{-1} , and ± 4 m s^{-1} , respectively.

3.4.1. Small-Scale Gravity Waves

Siskind et al. (2010) showed the change in GW drag at mesospheric altitudes during the prolonged 2006 SSW, an event similar to what occurred in January 2013. Consistent with that work, Figure 6 contrasts the evolution of the modeled zonal mean GW drag and MLT circulation between the 2012–2013 and 2013–2014 winters. Prior to the SSW/MC, modeled GW drag is primarily westward in the Northern Hemisphere (except above 70°N) during late December 2012. After the onset of the SSW/MC, the strong eastward GW drag of at least $40 \text{ m s}^{-1} \text{ day}^{-1}$ extends down into the tropics, with local maxima of $\sim 90 \text{ m s}^{-1} \text{ day}^{-1}$ calculated at middle to high northern latitudes. No such sharp increase in GW drag is modeled for in the 2013–2014 winter when neither a SSW or MC occurred.

This enhancement in eastward GW drag during the initial SSW phase is driven by a reversal in the zonal mean zonal winds from eastward to westward at high latitudes in the middle atmosphere (see Figure S7 in the supporting information), thereby filtering out westward propagating GWs and preferentially allowing eastward propagating GWs to reach the MLT (Chandran et al., 2011; de Wit et al., 2014; McLandress et al., 2013; Siskind et al., 2010; Limpasuvan et al., 2016). There, these eastward propagating GW break and

dissipate imparting their eastward momentum into the zonal mean flow, as evidenced by the 20–40 m s^{−1} increase seen in modeled zonal winds between 7 and 14 January 2013. Again, although there are periodic increases in zonal mean zonal winds, there is not a dramatic change in the zonal mean zonal circulation during the 2013–2014 winter.

Initially, increased eastward GW forcing acts to drive increased eastward zonal mean zonal winds, ultimately inducing a strong change in the modeled meridional residual circulation (\bar{v}^* in Figure 6c, see for its derivation Andrews et al., 1987) with enhanced equatorward (and upward, not shown) flow around 100 km, consistent with MR observations (see Li et al., 2020). Through continuity, this residual circulation leads to a net divergence of light species and subsequent high-latitude decrease in [O], [He], and [H] for the 2012–2013 SSW/MC event, amplifying the expected seasonal decreases (see Figure 3). It also follows that this residual equatorward and upward flow produces strong adiabatic cooling in the mesopause region during the initial phase of the January 2013 event (see Figure 10 below).

To further quantify the role small-scale GWs play in decreasing light species densities in the middle and upper atmosphere, we performed a numerical experiment for the 2012–2013 northern winter months in which the TIME-GCM middle atmosphere up to ~97 km (i.e., model log-pressure level −7) is still constrained by NAVGEM-HA analysis/forecasts, but the TIME-GCM subgrid-scale GW parameterization is turned off. Turning the TIME-GCM GW parameterization off removes the GW drag terms from model momentum (and temperature) equations, and replaces the eddy diffusivities of mass, momentum, and energy with a height-dependent Rayleigh damping term. Although the TIME-GCM GW parameterization is turned off in the “No GWs” simulation, the NAVGEM-HA fields used to constrain TIME-GCM between ~30 and 97 km still include GW effects; therefore, we could not completely remove GW impacts on TIME-GCM light species. However, above ~80 km the one-way coupling between TIME-GCM and NAVGEM-HA is relatively weak (~25% and decreasing with increasing altitude, see Figure S1a), such that small-scale GW forcing of NAVGEM-HA fields should not have a large effect on our TIME-GCM winds via nudging.

Figure 7 depicts the modeled zonal and diurnal mean atomic hydrogen abundance between 75°N and 80°N in January 2013, as well as the SSW/MC induced changes in light species and N₂ in the mesosphere and thermosphere for a TIME-GCM simulation in which the GW parameterization is turned off. The sharp upward buckling zonal mean H contours are not present in Figure 7a after SSW/MC onset when GWs are excluded from TIME-GCM, indicating that light species depletions in the high-latitude MLT region are strongly driven by changes in GW forcing. Above ~100 km, the overall magnitudes in the change to the light species and N₂ number density due to SSW/MC conditions in the “No GWs” simulations are about half of those in the simulation including GWs. Midlatitude increases in helium and hydrogen associated with the January 2013 SSW/MC are also reduced when parameterized GWs are excluded from our TIME-GCM simulation. Therefore, we conclude that midlatitude enhancements and high-latitude depletions in light species between ~90 and 110 km are strongly driven by the changes in the GW propagation associated with the SSW/MC event. Also, these same GW changes account for about half of the light species and N₂ variability extending from the lower thermosphere up to the exobase during the January 2013 SSW/MC event.

3.4.2. Migrating Semidiurnal Tide

Because SSWs originate in a layer of the atmosphere where ozone heating is important (e.g., Nath et al., 2015), it has been suggested that changes in the migrating semidiurnal tide (SW2) could be responsible for some of the changes seen at higher altitudes (e.g., Goncharenko et al., 2012; Jin et al., 2012; Pedatella & Forbes, 2010; Siddiqui et al., 2019). Thus, it is important to assess to what extent SW2 changes might be responsible for the remaining SSW/MC light species depletions seen in our TIME-GCM simulation excluding small-scale GW forcing. Unfortunately, with the TIME-GCM SW2 is generated internally within the stratosphere and lower mesosphere of the model (Hagan, 1996) and cannot be straightforwardly isolated. The same can be said for separating SW2 from the lunar semidiurnal tide in our model simulations. Specifically, our TIME-GCM simulations did not encompass a long enough time period to completely separate the SW2 from the lunar semidiurnal tide that enters the model via nudging to NAVGEM-HA analysis/forecast fields. Therefore, we cannot completely rule out aliasing from the lunar semidiurnal tide into modeled SW2 amplitudes and phases that were calculated using a Fourier decomposition of hourly TIME-GCM output. However, we suspect that the contribution from aliasing by the lunar semidiurnal tide into our calculated SW2 amplitudes and phases to be fairly small (see Stober et al., 2019). Nonetheless, we can assess to what extent the predominant semidiurnal wave forcing or SW2, differs between the three cases we have simulated (2012–2013 with and without GW and 2013–2014). This is shown in Figure 8.

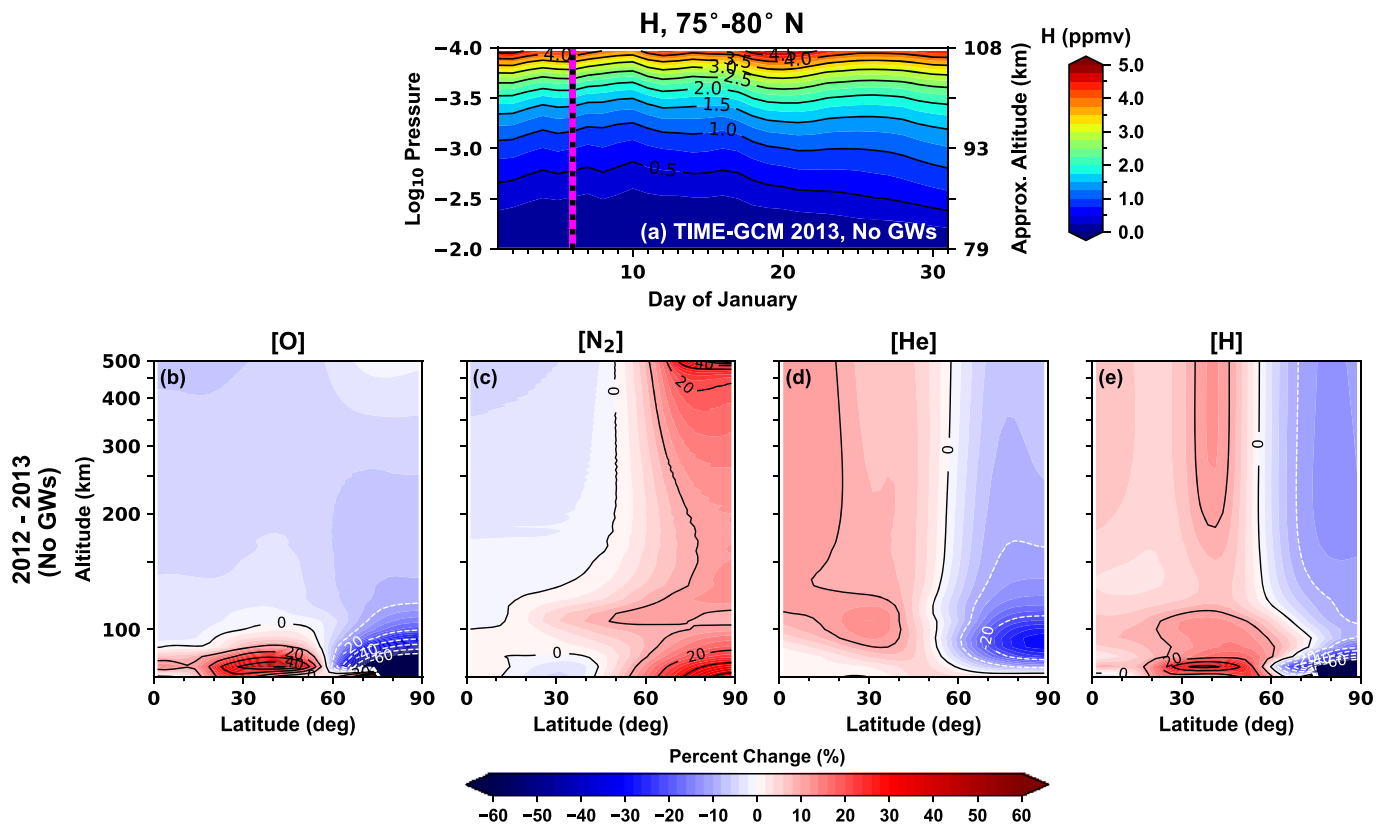


Figure 7. (a) Same as Figure 3f and (b–e) are the same as Figures 4a–4d, except from a TIME-GCM simulation with the subgrid-scale gravity wave parameterization turned off.

Figure 8 reveals the potential role of enhanced SW2 forcing on the zonal mean winds and meridional residual circulation at ~ 115 km in our three different TIME-GCM simulations. Note, dynamical results in Figure 8 are shown at a higher pressure level than those shown in Figure 6 because tidal effects on thermospheric composition are most effective at altitudes close to and above where they reach their maximum amplitudes. At these altitudes large eastward zonal mean zonal wind enhancements between 7 and 14 January 2013 are effectively removed at the onset of the SSW and MC when the model GW parameterization is turned off. However, after 15 January 2013, there is a strong increase in the low-to-middle latitude westward mean winds in both 2012–2013 simulations (with and without GWs). This westward wind increase corresponds to an increase in the magnitude of the SW2 amplitude which is not seen in 2014. The bottom panels (Figures 8c and 8f) show significant increases in the meridional residual wind in 2013 that are also absent in 2014. Taken together, the simultaneous occurrence of westward winds, enhanced SW2 amplitudes and increased poleward flow in both the 2012–2013 simulations and their absence in 2013–2014 is consistent with the idea that amplified SW2 forcing plays an important role in the momentum budget of the perturbed MLT during SSWs and MCs.

This enhanced poleward (and downward-not shown) flow driven at least in part by increased SW2 amplitudes between ~ 115 and 150 km acts to adiabatically heat the lower thermosphere, especially at middle-to-high northern latitudes (see Figure 10). Further, this enhanced poleward (and downward) flow shown in Figure 8 coupled with enhanced equatorward (and upward) flow shown in Figure 6 between ~ 90 and 110 km is consistent with previous modeling studies of enhanced lower atmospheric wave forcing on the meridional residual circulation (e.g., Miyoshi et al., 2015; Oberheide et al., 2020; Pedatella et al., 2016; Yamazaki & Richmond, 2013).

In order to more rigorously isolate the SW2 effects on light species depletions during a SSW/MC one must use a model whose lower boundary is above the stratosphere and lower mesosphere (i.e., not the TIME-GCM). Similar to simulations performed by Pedatella (2016), we forced the TIE-GCM, whose lower boundary is

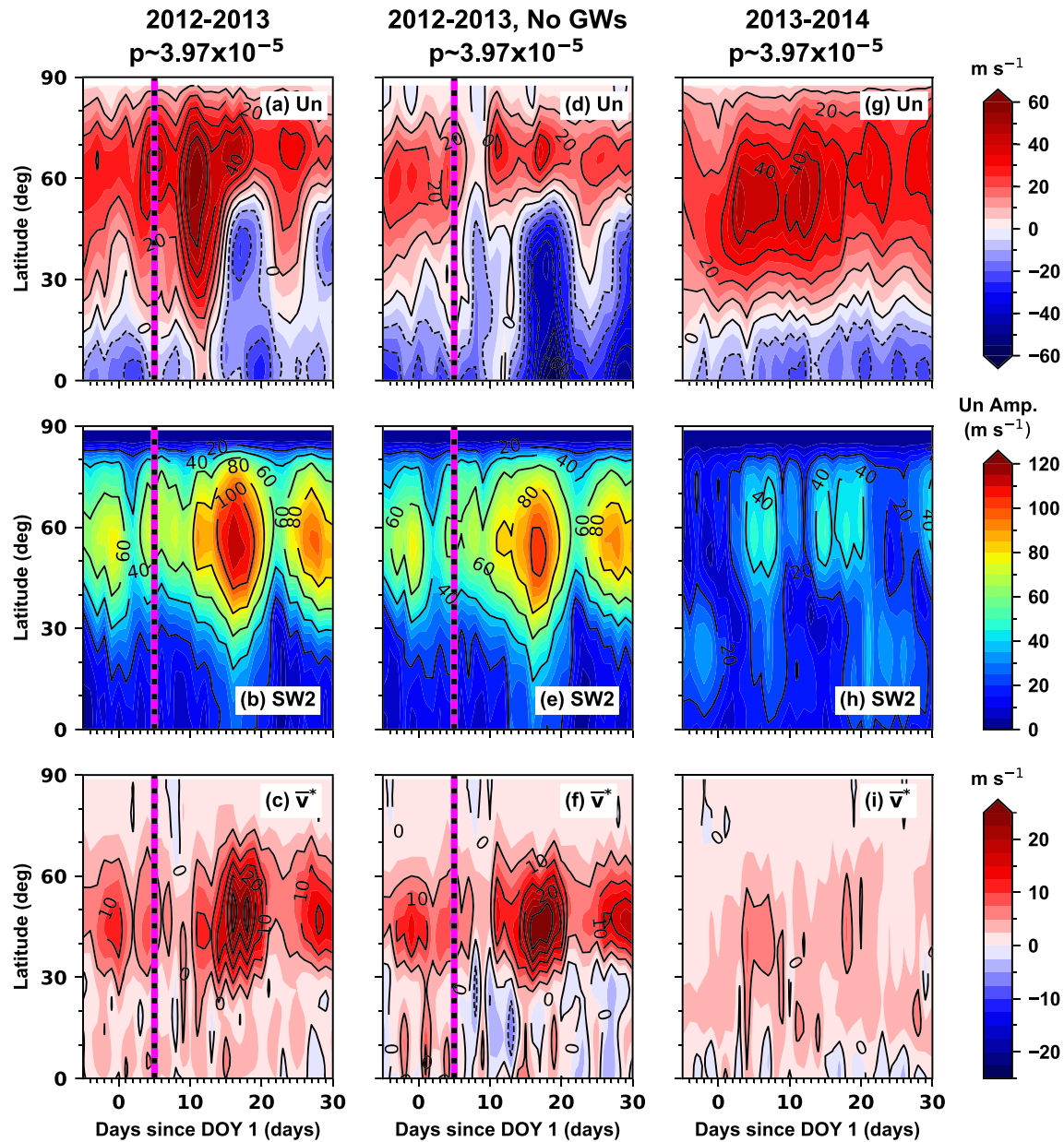


Figure 8. Time series of modeled zonal and diurnal mean zonal winds (a, d, and g), daily migrating semidiurnal tidal zonal wind amplitudes (b, e, and h), and the meridional residual circulation (\bar{v}^* , c, f, and i) from all model resolved waves in the Northern Hemisphere during the 2012–2013 winter with (first column) and without GWs (second column), as well as during the 2013–2014 winter (third column) at $\sim 3.97 \times 10^{-5}$ hPa or ~ 115 km. The magenta-black hatched vertical line on 6 January 2013 denotes SSW and MC onset. Un , SW2 amplitude, and \bar{v}^* are contoured every ± 10 , 20, and ± 5 $m s^{-1}$, respectively.

at ~ 97 km, with nudged TIME-GCM output during January 2013 using the same constant solar and geomagnetic inputs employed in our TIME-GCM numerical experiments. Specifically, we performed TIE-GCM numerical experiments where lower boundary horizontal winds, neutral temperatures, and geopotential heights were specified using hourly horizontal wind, neutral temperature, and geopotential height outputs at model log-pressure level -7 from our NAVGEM-HA nudged TIME-GCM with no GWs. Two different TIE-GCM simulations were performed, one which included TIME-GCM resolved-scale wave forcing, and a second that included all TIME-GCM resolved-scale wave forcing except SW2. Note that TIE-GCM does not have a parameterization for subgrid-scale GW, so that differences between TIE-GCM simulations with and without TIME-GCM SW2 forcing should elucidate the role of the migrating semidiurnal tide in the light species depletions seen in Figure 4.

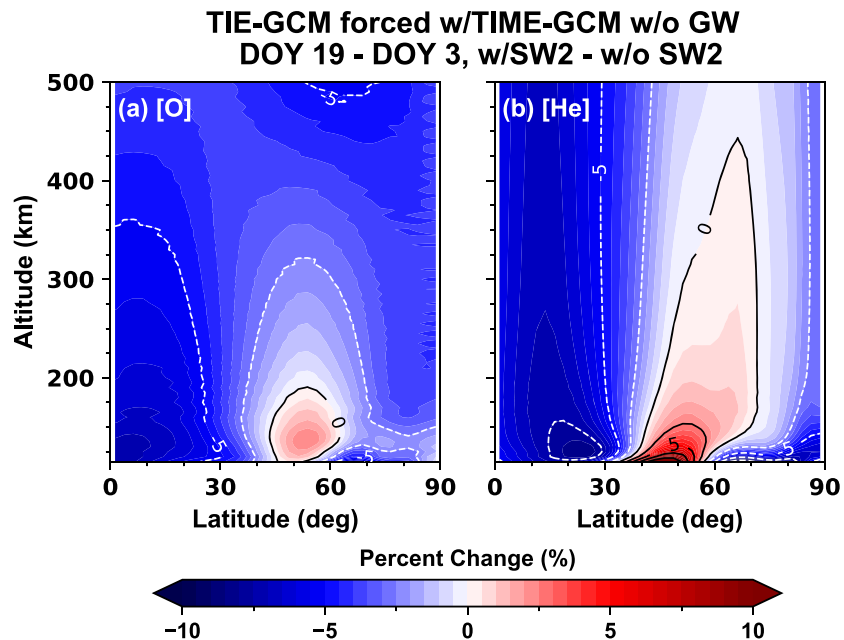


Figure 9. TIE-GCM Northern Hemispheric percent changes in [O] (a) and [He] (b) between 19 January 2013 and 3 January 2013 from simulations including and excluding SW2 lower boundary forcing as function of latitude and altitude. Percent changes are contoured every $\pm 5\%$.

Figure 9 shows the SW2 induced changes in [O] and [He] during the January 2013 SSW/MC as function of altitude in the Northern Hemisphere. Differences fields were calculated between 19 January 2013, where the SW2 reached its maximum amplitude during the SSW/MC event, and 3 January 2013, where the SW2 reached its minimum amplitude prior to SSW/MC onset (see Figure 8). The latitudinal distribution of [O] and [He] changes simulated in the TIE-GCM forced by the TIME-GCM are generally qualitatively consistent with those modeled by the nudged TIME-GCM, with the exception of tropical depletions of helium (see Figures 4 and 7). High-latitude depletions in [O] and [He] due to enhanced SW2 forcing during the January 2013 SSW/MC are on the order of -5 – 10% and extend well into the upper thermosphere, with similar magnitudes to the residual percent differences shown in Figure 7 when subgrid-scale GWs were turned off in TIME-GCM. This suggests that enhanced SW2 forcing during a SSW/MC does contribute to the light species depletions (and enhancements) at high (middle) northern latitudes, and demonstrates these SSW/MC changes in light species are not driven by GWs alone in TIME-GCM. Note, atomic hydrogen is not shown in Figure 9 because TIE-GCM does not solve a minor species continuity equation for atomic hydrogen.

3.4.3. Temperature and Composition Effects

Starting with Liu and Roble (2002), it is now understood that increases in high northern latitude lower thermospheric temperatures can occur in response to a SSW/MC event (see Funke et al., 2010). Figure 10 shows zonal mean temperature differences as a function of latitude and altitude in the Northern Hemisphere from our three different TIME-GCM simulations. Most notably, we see a pronounced layer of warming of 15 – 30 K poleward of 60°N in response to the SSW/MC. When GWs are removed this almost entirely disappears. This suggests that mesopause and thermospheric temperature changes in response to a SSW/MC are mainly driven by enhanced GW forcing, with enhanced SW2 forcing playing a secondary role. The temperature changes in 2013–2014 are more typical of the expected seasonal variations at high northern latitudes in the MLT and thermosphere and are at most ± 10 K (Figure 10c).

The temperature changes in Figure 10 are important because, combined with composition differences shown earlier, can impact thermospheric light species in addition to the dynamical changes discussed above. Thus, Kockarts (1972) expressed the vertical diffusion of light or minor species (He, H), through a

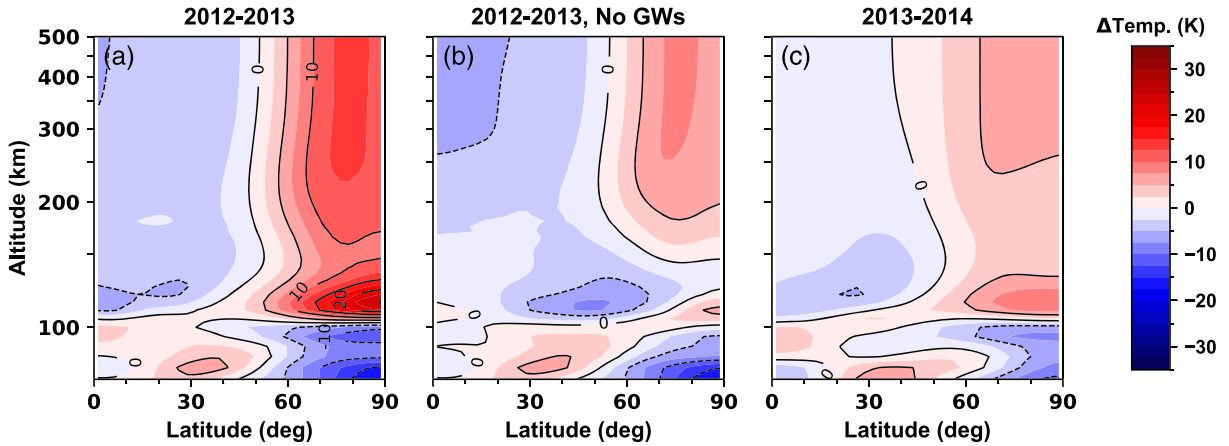


Figure 10. Zonal and diurnal mean temperature differences as a function of altitude in the Northern Hemisphere between the “disturbed” and “predisturbance” time periods from TIME-GCM simulations with (a) and without GWs (b, “No GWs”) in 2012–2013 and equivalent time periods in 2013–2014 (c). Temperature differences are contoured every ± 5 K.

thermosphere composed of major species (i.e., O, O₂, and N₂) as a diffusive separation velocity, including eddy and molecular diffusion

$$w_{Diff_i} = -D_i \left[\frac{1}{n_i} \frac{dn_i}{dz} + \frac{1}{H_i} + (1 + \alpha_i) \frac{1}{T} \frac{dT}{dz} \right] - K_{zz} \left[\frac{1}{n_i} \frac{dn_i}{dz} + \frac{1}{H} + \frac{1}{T} \frac{dT}{dz} \right], \quad (1)$$

where w_{Diff_i} is the total diffusive separation velocity between light species i through the background gas. D_i is the molecular diffusion coefficient, K_{zz} is the eddy diffusion coefficient, n_i is the number density of the i th species, $H = \frac{kT}{mg}$ is the pressure scale height of the background gas, $H_i = \frac{kT}{m_i g}$ is the light/minor species i pressure scale height, k is the Boltzmann constant, g is gravitational acceleration, T is the neutral temperature, α_i is thermal diffusion coefficient (the same constant for He and H), z is height, and m and m_i are the molecular weight of the background atmosphere and the mass of the i th light/minor species.

Given the scale height and vertical temperature gradient terms in Equation 1, it is clear that changes in temperature and composition in the thermosphere driven by SSWs and or MCs will affect the helium and atomic hydrogen distributions. Specifically, Kockarts (1972) demonstrated that increasing thermospheric temperature and eddy diffusion act to reduce light species densities in the thermosphere. Note that increased mixing associated with small-scale GW and SW2 induced meridional residual circulation setup in the lower thermosphere during a SSW and MC (see Figures 6 and 8 above) is analogous to increasing eddy mixing, which inhibits diffusive separation of species whose molecular weight is less than the mean atmospheric mass, resulting in lower light species densities in the thermosphere (e.g., Jones et al., 2014; Yamazaki & Richmond, 2013). Thus, taking the GW and SW2 effects on N₂ discussed earlier and temperature changes discussed above together, the full description of modeled light species depletions shown in Figure 4 emerge. Greater temperature increases, coupled with greater N₂ increases via increased scale heights, and lower thermospheric mixing account for the large depletions in He and H in our 2012–213 TIME-GCM simulations when including small-scale GWs.

Further evidence of different portions of the lower atmospheric wave spectrum driving light species depletions at high latitudes in our TIME-GCM simulations is offered in Figure 11. Shown are effective mass profiles of atomic hydrogen extending from the upper mesosphere to the middle thermosphere. The effective mass of a species (m_i^{eff}) was derived by Jones, Emmert, et al. (2018) and given by the following equation:

$$m_i^{eff} = \bar{m} \left[\frac{d(\ln n_i)}{d(\ln p)} + \frac{d(\ln T)}{d(\ln p)} \right]. \quad (2)$$

\bar{m} is the mean molecular mass, n_i is the number density of species i , p is pressure, and T is the neutral temperature. Essentially, the effective mass is a diagnostic that assesses the behavior of a species profile relative to diffusive equilibrium. If a species effective mass is heavier than the actual species mass that species density is decreasing faster with altitude than is predicted by diffusive equilibrium, representing a sink of

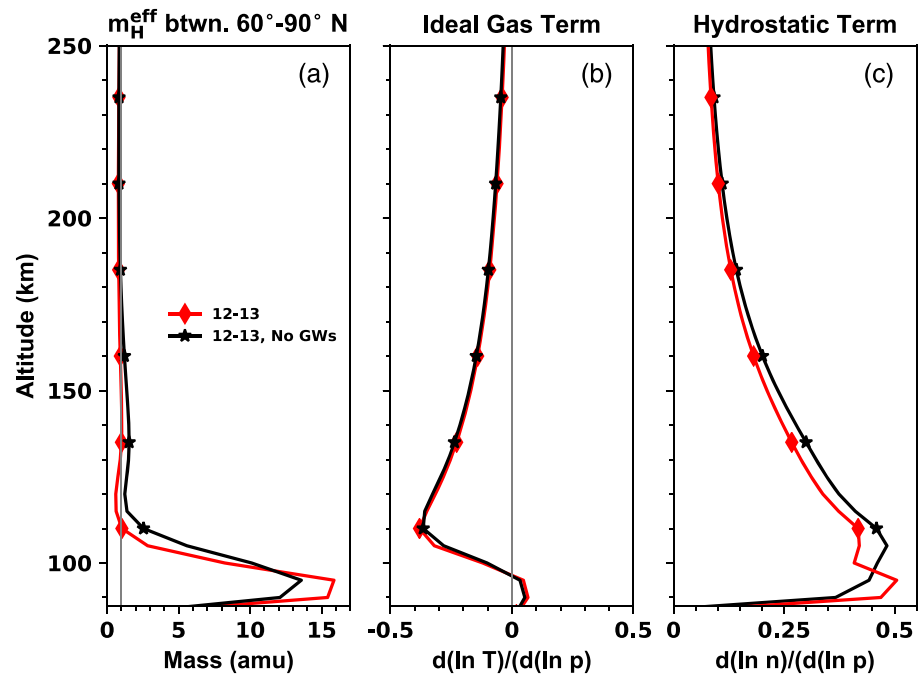


Figure 11. Atomic hydrogen effective mass profiles averaged during the “disturbed” time period and between 60°N and 90°N from TIME-GCM simulations with (red diamonds) and without GWs (black stars) in 2012–2013. Shown are the total effective mass of atomic hydrogen (m_H^{eff} , a), the first term of Equation 2 or the ideal gas term (b), and the second term of Equation 2 or the hydrostatic term (c).

that species. Oppositely, where the effective mass of the i th species is less than its actual mass represents a source of that species. The effective mass, though, does not identify the physical processes that cause a species to depart from diffusive equilibrium, therefore one must have some insight into the processes responsible for altering a species distribution relative to diffusive equilibrium.

The effective mass of H calculation shown in Figure 11a is consistent with our theme throughout, which is the strong H depletion in the mesopause region is greatly affected by a change in the GW activity. When small-scale GWs are excluded from the TIME-GCM, the effective mass of H is less than when small-scale GWs are included, indicating that H depletions in the no-GWs case are weaker. From an effective mass perspective when the GWs are turned off, the temperature effect is almost equivalent between the two cases above the mesopause (Figure 11b). The hydrostatic term, which includes the concomitant effects of thermodynamics and chemistry, shows that there are changes when the GW parameterization is neglected. Removing the GWs acts to keep the hydrostatic term and ultimately the effective mass of profile of H greater than 1 amu. This implies the H (and He) depletion will be present even without GWs in the TIME-GCM during strong middle atmospheric dynamical events because other parts of the lower atmospheric wave spectrum (i.e., SW2) are playing a role.

3.5. Ionospheric Impact

The changes in neutral composition as well as the changes in tidal forcing that we have documented will naturally have implications for the ionosphere through ion-neutral coupling (e.g., Pedatella et al., 2016; Siskind et al., 2014, and many others) that could extend well above the model domain into the exosphere and plasmasphere. This is seen in Figure 12, which shows the percent changes in $[O^+]$ and $[H^+]$ due to SSW and MC variability during the northern winter of 2012–2013 and general seasonal variability in the absence of a middle atmospheric dynamical event in the 2013–2014 northern winter. The general reduction in $[O^+]$ over all northern latitudes during the January 2013 SSW/MC is consistent with the decrease in O/N_2 simulated herein, and by Pedatella et al. (2016), as well as what has been observed by Oberheide et al. (2020). Additionally, we show H^+ depletions of 15% or more extending well into the upper thermosphere at high latitudes during the January 2013 SSW/MC. By contrast, the changes seen in these constituents for the 2013–2014 year, when no SSW/MC occurred, are much smaller.

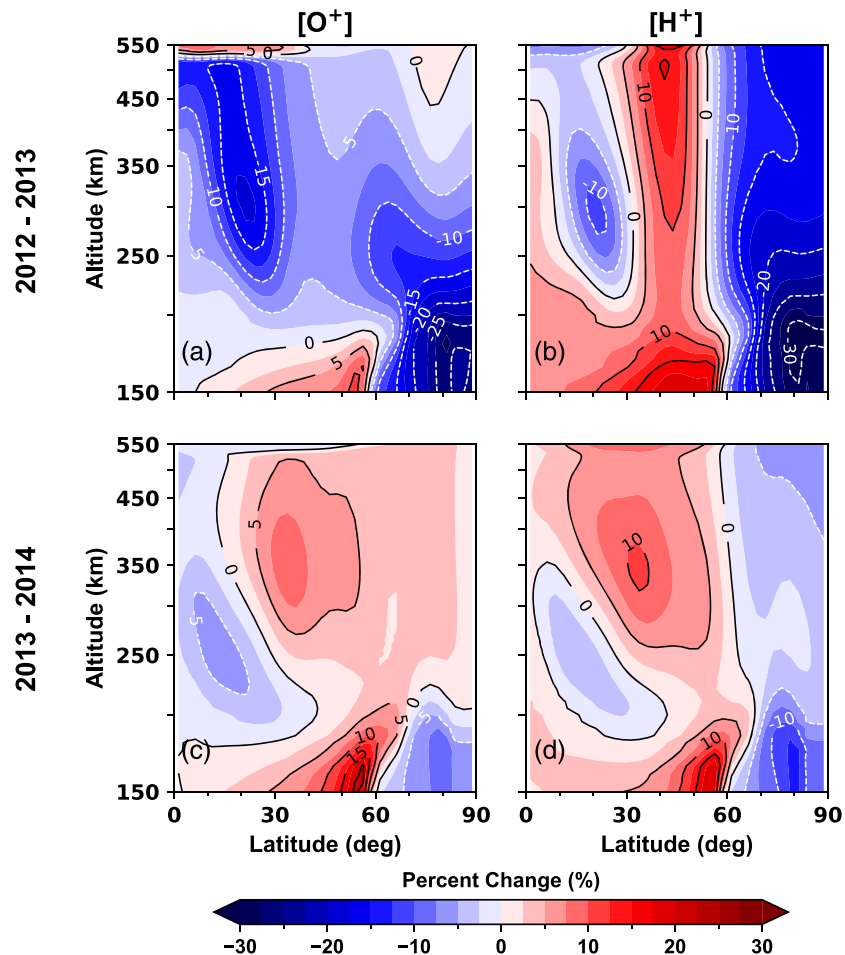


Figure 12. Percent changes in TIME-GCM zonally averaged $[O^+]$ (a and c) and $[H^+]$, (b and d) as function of altitude in the Northern Hemisphere between the “disturbed” and “predisturbance” time periods in 2012–2013 (top row) and equivalent time periods in 2013–2014 (bottom row). Differences are contoured every $\pm 5\%$.

Increases in H^+ of ~ 10 – 15% at midlatitudes appear in both winter seasons indicating this is more of a seasonal feature, with perhaps the SSW/MC contributing, but only weakly. There is a secondary depletion of H^+ at low latitudes ($<30^\circ N$) consistent with large O^+ depletions (which have been observed via changes in electron density and total electron content for a decade or more now, e.g., Goncharenko et al., 2010), but this is weaker than those modeled at high northern latitudes during the January 2013 SSW/MC. Finally, it is interesting to note that these O^+ and H^+ changes extend up to the top of the thermosphere. Given that H and H^+ become major constituents above the thermosphere and that Krall et al. (2016) have already demonstrated that the day-to-day variations in thermospheric composition (and winds) could have a large effect on plasmasphere refilling after a geomagnetic storm, we speculate that the effects of the SSW/MC might drive variability out into the plasmasphere. Storms lead to the outer plasmasphere being stripped away such that the plasmopause reaches L values of order 2.5 to 3.0, equivalent to latitudes of between about 50° and 55° . The H^+ density is much higher at the top of the thermosphere following the SSW/MC in this latitude range (Figure 12), which could potentially result in faster refilling of those magnetic flux tubes following a magnetic storm coincident with a SSW/MC event.

4. Summary and Conclusions

Through a combined data and modeling approach, we have shown the effects of sudden stratospheric warming and mesospheric cooling events on the atomic oxygen and light species distributions in the upper mesosphere, thermosphere, and potentially the exosphere, topside ionosphere, and plasmasphere. Using a set of TIME-GCM numerical experiments constrained by NAVGEM-HA in the middle atmosphere during

the 2012–2013 northern winter period, as well as TIE-GCM numerical experiments, we quantify the role different portions of the SSW/MC altered wave spectrum play on generating these changes in O, He, and H at thermospheric altitudes. The following important results and conclusions to emerge from this study were:

1. TIME-GCM constrained by NAVGEM-HA is capable of reproducing the observed atomic H variability from TIMED/SABER and observed globally averaged thermospheric mass density decreases associated with SSWs and MCs. Specifically, both SABER and TIME-GCM show that high northern latitude decreases in MLT atomic hydrogen commence with mesospheric cooling onset, rather than SSW onset, for some major SSW and MC events, including the 2006, 2009, and 2013 event. Orbit-derived density superposed epoch analysis and TIME-GCM both show a 5–7% decrease in global average mass density in the upper thermosphere during a SSW and MC, which is driven by the combined effects of temperature and composition.
2. Sudden stratospheric warming and mesospheric cooling induced reductions in O, He, and H extend from the mesopause to the top boundary of the TIME-GCM, with the largest depletions modeled at northern polar latitudes, acting to reduce the typical light species accumulations in the winter hemisphere. We found that the lighter the species (i.e., the biggest difference between a species mass and the mean mass of the background atmosphere), the larger the high-latitude depletion was. These depletions were driven by enhanced small-scale gravity wave and migrating semidiurnal tidal forcing and associated meridional residual mean circulation changes in the MLT. The increased mixing driven by the residual mean circulation acts to remove light species from the thermosphere while increasing N₂ thereby allowing He and H depletions to project well into the thermosphere. Ultimately, increased eastward small-scale GWs dissipation/breaking during the January 2013 SSW/MC event appears to be the primary driver of light species depletions, with increased SW2 activity playing a modest role in the TIME-GCM. With the recent launch of the Global-scale Observations of the Limb and Disk (GOLD) mission studies using SABER H and GOLD O/N₂ (e.g., Oberheide et al., 2020) can be used to trace the effects of SSWs and MCs both vertically and horizontally within the atmosphere. These data provide the first opportunity to examine coupling from the high-latitude stratosphere to the tropical thermosphere.
3. Light species variability associated with SSW/MC may potentially affect the plasma population of the topside ionosphere and plasmasphere. Notable H⁺ variability of ±10–20% is modeled for during the January 2013 SSW/MC. This suggests that middle atmospheric dynamics could influence the cold plasma population of the inner magnetosphere, even though the two regions are separated by multiple earth radii.

The last point above motivates future observational and modeling efforts to extend out into the exosphere, geocorona, and inner magnetosphere. In order to do so, coupling a model like TIME-GCM that models the continuum fluid regime of the middle and upper atmosphere to a Monte Carlo type model (e.g., Hodges Jr. 1994) that uses the motion of particle populations to perform simulations of nonequilibrium gas dynamics, or an ionospheric model like SAMI3 (SAMI3 is also a model of the ionosphere, Huba & Krall, 2013) is required. This hierarchical approach to modeling would allow the aeronomy community to probe exospheric and inner magnetospheric variability whose origins lie in the lower and middle atmosphere in a novel way.

Acronyms

Below we have listed the acronyms used to improve the readability of this paper.

CMOR,	Canadian Meteor Orbit Radar
DMSP,	Defense Meteorological Satellite Program
EUV,	Extreme ultraviolet
EUVAC,	EUV flux model for aeronomic calculations
F10.7,	10.7 cm solar radio flux
FUV,	Far ultraviolet
GAMDM,	Global Average Mass Density Model
GAIA,	Ground-to-topside Atmosphere and Ionosphere for Aeronomy
GOLD,	Global-scale Observations of the Limb and Disk
GW,	Gravity Wave
MC,	Mesospheric cooling
MLS,	Microwave Limb Sounder

MLT,	Mesosphere and lower thermosphere
MR,	Meteor radar
NAVGEN-HA,	Navy global environmental model a high-altitude version
NCAR,	National Center for Atmospheric Research
NO _x ,	Odd nitrogen species
NOGAPS-ALPHA,	Navy operational global atmospheric prediction system-advanced level physics high altitude forecast model
SABER,	Sounding of the atmosphere using broadband emission radiometry
SAMI3,	Sami3 is Also a Model of the Ionosphere
SSMIS,	Special Sensor Microwave Imager/Sounder
SSW,	Sudden stratospheric warming
SW2,	Semidiurnal migrating tide with zonal wave number 2
TGCM,	Thermospheric general circulation model
TI,	Thermosphere-ionosphere
TIE-GCM,	Thermosphere-ionosphere-electrodynamics general circulation model
TIME-GCM,	Thermosphere-ionosphere-mesosphere-electrodynamics general circulation model
TIMED,	Thermosphere ionosphere mesosphere energetics and dynamics

Data Availability Statement

The TIME-GCM code is made available by contacting the National Center for Atmospheric Research. The TIE-GCM code is available for download at <https://www.hao.ucar.edu/modeling/tgcm/>. The model output produced herein is reproducible from the TGCM model source code following the discussions and implementations of the nudging schemes and lower boundary conditions described thoroughly in sections 2 and 3, as well as the supporting information. Daily NCAR TGCMs outputs in netCDF format from this study are archived on the DoD HPCMP long-term storage system. NAVGEN-HA inputs used to constrain the stratosphere and mesosphere of the TIME-GCM simulations performed herein are accessible at <https://map.nrl.navy.mil> (cd to map/pub/nrl/jgrspace2020/lightspecies/navgem/djfm1213 or map/pub/nrl/jgrspace2020/lightspecies/navgem/djfm1314). Data from the Sodankylä meteor radar (SGO) used herein are available at https://www.sgo.fi/pub/JGR_SSW_2013 <https://www.sgo.fi/pub/cd> to JGR_SSW_2013/HWD_201301 or JGR_SSW_2013/HWD_201401). Access to data from the CMOR and Collm meteor radars is discussed in Stober et al. (2019). SABER atomic hydrogen data are available at <http://saber.gats-inc.com/data.php> then by clicking on the ftp://saber.gats-inc.com/Version2_0/Level2A/link. Orbit-derived global average mass density data and the GAMDM model parameters are available in the supporting information of Emmert (2015). The SSW epochs used to generate the superposed epoch analysis in Figure 5 herein are in the supporting information of Yamazaki et al. (2015). Finally, all model and satellite data shown in Figures S2–S7 can be accessed using the data links provided above.

References

- Andrews, D., Holton, J., & Leovy, C. (1987). *Middle atmosphere dynamics* (pp. 113–130). San Diego, CA: Academic Press.
- Bates, D. R., & Nicolet, M. (1950). The photochemistry of atmospheric water vapor. *Journal of Geophysical Research*, 55(3), 301–327. <https://doi.org/10.1029/JZ055i003p00301>
- Brasseur, G., & Solomon, S. (2005). *Aeronomy of the middle atmosphere: Chemistry and physics of the stratosphere and mesosphere*. Dordrecht, Netherlands: Springer. Retrieved from <https://books.google.com/books?id=HoV1VNFJwVwC>
- Brown, P., Weryk, R., Wong, D., & Jones, J. (2008). A meteoroid stream survey using the Canadian Meteor Orbit Radar: I. Methodology and radiant catalogue. *Icarus*, 195(1), 317–339. <https://doi.org/10.1016/j.icarus.2007.12.002>
- Catling, D. C., & Kasting, J. F. (2017). *Atmospheric evolution on inhabited and lifeless worlds*. Cambridge, UK: Cambridge University Press. <https://doi.org/10.1017/9781139020558>
- Chandran, A., Collins, R. L., Garcia, R. R., & Marsh, D. R. (2011). A case study of an elevated stratopause generated in the Whole Atmosphere Community Climate Model. *Geophysical Research Letters*, 38, L08804. <https://doi.org/10.1029/2010GL046566>
- Chau, J. L., Goncharenko, L. P., Fejer, B. G., & Liu, H. L. (2012). Equatorial and low latitude ionospheric effects during sudden stratospheric warming events. *Space Science Reviews*, 168(1), 385–417. <https://doi.org/10.1007/s11214-011-9797-5>
- Coy, L., Eckermann, S. D., Hoppel, K. W., & Sassi, F. (2011). Mesospheric precursors to the major stratospheric sudden warming of 2009: Validation and dynamical attribution using a ground-to-edge-of-space data assimilation system. *Journal of Advances in Modeling Earth Systems*, 3, 4. <https://doi.org/10.1029/2011MS000067>
- Coy, L., Siskind, D. E., Eckermann, S. D., McCormack, J. P., Allen, D. R., & Hogan, T. F. (2005). Modeling the August 2002 minor warming event. *Geophysical Research Letters*, 32, L07808. <https://doi.org/10.1029/2005GL022400>
- de Wit, R. J., Hibbins, R. E., Espy, P. J., Orsolini, Y. J., Limpasuvan, V., & Kinnison, D. E. (2014). Observations of gravity wave forcing of the mesopause region during the January 2013 major sudden stratospheric warming. *Geophysical Research Letters*, 41, 4745–4752. <https://doi.org/10.1002/2014GL060501>

Acknowledgments

This work was supported by the NASA Heliophysics Supporting Research (NNH16ZDA001N-HSR/ITM16_2-0013) and Early Career Investigator (NNH18ZDA001N-ECIP/18-ECIP_2-0018) Programs. D. E. Siskind and M. G. Mlynczak acknowledge support from the NASA/TIMED SABER project (Interagency Purchase Request NNG17PX04I to NRL). J. P. McCormack acknowledges support from NASA Grant NNH18ZDA001N. J. T. Emmert acknowledges support from the Chief of Naval Research. M. S. Dhady acknowledges support from the NASA ECI and Living with a Star (NNH18ZDA001N/18-LWS18_2-0126) Programs. H. E. Attard was an NRC Postdoctoral Research Associate at the U.S. Naval Research Laboratory and was supported by the Chief of Naval Research. The authors would like to acknowledge Eric Sutton and Jeffrey Thayer for thoughtful initial discussions regarding this project. The authors would also like to express gratitude to DeAndre A. Johnson who initially worked with some of the TIME-GCM output discussed herein as part of the Naval Research Laboratory Research Internship Program HBCU/MI/TCU Undergraduates, Graduates, and Post-Doctoral Students. Computational resources for this work were provided by the U. S. Department of Defense (DoD) High Performance Computing Modernization Program (HPCMP).

- Dickinson, R. E., Ridley, E. C., & Roble, R. G. (1984). Thermospheric general circulation with coupled dynamics and composition. *Journal of the Atmospheric Sciences*, 41(2), 205–219. [https://doi.org/10.1175/1520-0469\(1984\)041<0205:TGCWCD>2.0.CO;2](https://doi.org/10.1175/1520-0469(1984)041<0205:TGCWCD>2.0.CO;2)
- Eckermann, S. D., Ma, J., Hoppel, K. W., Kuhl, D. D., Allen, D. R., Doyle, J. A., et al. (2018). High-altitude (0–100 km) global atmospheric reanalysis system: Description and application to the 2014 austral winter of the deep propagating gravity wave experiment (DEEPWAVE). *Monthly Weather Review*, 146(8), 2639–2666. <https://doi.org/10.1175/MWR-D-17-0386.1>
- Emery, B., Roble, R. G., Ridley, E., Richmond, A., Knipp, D., Crowley, G., et al. (2012). Parameterization of the ion convection and the auroral oval in the NCAR thermospheric general circulation models (*Technical Report*). Boulder, CO: National Center for Atmospheric Research. <https://doi.org/10.5065/D6N29TXZ>
- Emmert, J. T. (2009). A long-term data set of globally averaged thermospheric total mass density. *Journal of Geophysical Research*, 114, A06315. <https://doi.org/10.1029/2009JA014102>
- Emmert, J. T. (2015). Altitude and solar activity dependence of 1967–2005 thermospheric density trends derived from orbital drag. *Journal of Geophysical Research: Space Physics*, 120, 2940–2950. <https://doi.org/10.1002/2015JA021047>
- Emmert, J. T., & Picone, J. M. (2010). Climatology of globally averaged thermospheric mass density. *Journal of Geophysical Research*, 115, A09326. <https://doi.org/10.1029/2010JA015298>
- Evans, D. S. (1987). Global statistical patterns of auroral phenomena. *Proceedings of the Symposium on Quantitative Modeling of Magnetospheric-Ionospheric Coupling Processes* (pp. 325–330). Kyoto, Japan.
- Funke, B., Ball, W., Bender, S., Gardini, A., Harvey, V. L., Lambert, A., & Yushkov, V. (2017). HEPPA-II model–measurement intercomparison project: EPP indirect effects during the dynamically perturbed NH winter 2008–2009. *Atmospheric Chemistry and Physics*, 17(5), 3573–3604. <https://doi.org/10.5194/acp-17-3573-2017>
- Funke, B., López-Puertas, M., Bermejo-Pantaleón, D., García-Comas, M., Stiller, G. P., von Clarmann, T., & Linden, A. (2010). Evidence for dynamical coupling from the lower atmosphere to the thermosphere during a major stratospheric warming. *Geophysical Research Letters*, 37, L13803. <https://doi.org/10.1029/2010GL043619>
- Goncharenko, L. P., Chau, J. L., Liu, H. L., & Coster, A. J. (2010). Unexpected connections between the stratosphere and ionosphere. *Geophysical Research Letters*, 37, L10101. <https://doi.org/10.1029/2010GL043125>
- Goncharenko, L. P., Coster, A. J., Plumb, R. A., & Domeisen, D. I. V. (2012). The potential role of stratospheric ozone in the stratosphere-ionosphere coupling during stratospheric warmings. *Geophysical Research Letters*, 39, L08101. <https://doi.org/10.1029/2012GL051261>
- Goncharenko, L. P., Coster, A. J., Zhang, S. R., Erickson, P. J., Benkevitch, L., Aponte, N., & Hernández-Espiet, A. (2018). Deep ionospheric hole created by sudden stratospheric warming in the nighttime ionosphere. *Journal of Geophysical Research: Space Physics*, 123, 7621–7633. <https://doi.org/10.1029/2018JA025541>
- Hagan, M. E. (1996). Comparative effects of migrating solar sources on tidal signatures in the middle and upper atmosphere. *Journal of Geophysical Research*, 101(D16), 21,213–21,222. <https://doi.org/10.1029/96JD01374>
- Heelis, R. A., Lowell, J. K., & Spiro, R. W. (1982). A model of the high-latitude ionospheric convection pattern. *Journal of Geophysical Research*, 87(A8), 6339–6345. <https://doi.org/10.1029/JA087iA08p06339>
- Hocking, W., Fuller, B., & Vandeppeer, B. (2001). Real-time determination of meteor-related parameters utilizing modern digital technology. *Journal of Atmospheric and Solar-Terrestrial Physics*, 63(2), 155–169. [https://doi.org/10.1016/S1364-6826\(00\)00138-3](https://doi.org/10.1016/S1364-6826(00)00138-3)
- Hodges Jr., R. R. (1994). Monte Carlo simulation of the terrestrial hydrogen exosphere. *Journal of Geophysical Research*, 99(A12), 23,229–23,247. <https://doi.org/10.1029/94JA02183>
- Hogan, T. F., Liu, M., Ridout, J. A., Peng, M. S., Whitcomb, T. R., Ruston, B. C., et al. (2014). The navy global environmental model. *Oceanography*, 27, 116–125. <https://doi.org/10.5670/oceanog.2014.73>
- Huba, J., & Krall, J. (2013). Modeling the plasmasphere with SAMI3. *Geophysical Research Letters*, 40, 6–10. <https://doi.org/10.1029/2012GL054300>
- Hunten, D. M., & Strobel, D. F. (1974). Production and escape of terrestrial hydrogen. *Journal of the Atmospheric Sciences*, 31(2), 305–317. [https://doi.org/10.1175/1520-0469\(1974\)031<0305:PAEOTH>2.0.CO;2](https://doi.org/10.1175/1520-0469(1974)031<0305:PAEOTH>2.0.CO;2)
- Ismail, S., & Cogger, L. L. (1982). Temporal variations of polar cap OI 5577-Å airglow. *Planetary and Space Science*, 30(9), 865–873. [https://doi.org/10.1016/0032-0633\(82\)90129-5](https://doi.org/10.1016/0032-0633(82)90129-5)
- Jacobi, C. (2012). 6 year mean prevailing winds and tides measured by VHF meteor radar over Collm (51.3°N, 13.0°E). *Journal of Atmospheric and Solar-Terrestrial Physics*, 78–79, 8–18. <https://doi.org/10.1016/j.jastp.2011.04.010>
- Jin, H., Miyoshi, Y., Pancheva, D., Mukhtarov, P., Fujiwara, H., & Shinagawa, H. (2012). Response of migrating tides to the stratospheric sudden warming in 2009 and their effects on the ionosphere studied by a whole atmosphere-ionosphere model GAIA with COSMIC and TIMED/SABER observations. *Journal of Geophysical Research*, 117, A10323. <https://doi.org/10.1029/2012JA017650>
- Jones, M., Emmert, J. T., Drob, D. P., & Siskind, D. E. (2017). Middle atmosphere dynamical sources of the semiannual oscillation in the thermosphere and ionosphere. *Geophysical Research Letters*, 44, 12–21. <https://doi.org/10.1002/2016GL071741>
- Jones, M. Jr., Drob, D. P., Siskind, D. E., McCormack, J. P., Maute, A., McDonald, S. E., & Dymond, K. F. (2018). Evaluating different techniques for constraining lower atmospheric variability in an upper atmosphere general circulation model: A case study during the 2010 sudden stratospheric warming. *Journal of Advances in Modeling Earth Systems*, 10, 3076–3102. <https://doi.org/10.1029/2018MS001440>
- Jones, M. Jr., Emmert, J. T., Drob, D. P., Picone, J. M., & Meier, R. R. (2018). Origins of the thermosphere-ionosphere semiannual oscillation: Reformulating the “thermospheric spoon” mechanism. *Journal of Geophysical Research: Space Physics*, 123, 931–954. <https://doi.org/10.1002/2017JA024861>
- Jones, M. Jr., Forbes, J. M., & Hagan, M. E. (2014). Tidal-induced net transport effects on the oxygen distribution in the thermosphere. *Geophysical Research Letters*, 41, 5272–5279. <https://doi.org/10.1002/2014GL060698>
- Joshi, P. P., Phal, Y. D., & Waldrop, L. S. (2019). Quantification of the vertical transport and escape of atomic hydrogen in the terrestrial upper atmosphere. *Journal of Geophysical Research: Space Physics*, 124, 10,468–10,481. <https://doi.org/10.1029/2019JA027057>
- Keating, G., & Prior, E. (1968). The winter helium bulge. *Space Research*, 8, 982.
- Kockarts, G. (1972). Distribution of hydrogen and helium in the upper atmosphere. *Journal of Atmospheric and Terrestrial Physics*, 34(10), 1729–1743. [https://doi.org/10.1016/0021-9169\(72\)90032-3](https://doi.org/10.1016/0021-9169(72)90032-3)
- Krall, J., Emmert, J. T., Sassi, F., McDonald, S. E., & Huba, J. D. (2016). Day-to-day variability in the thermosphere and its impact on plasmasphere refilling. *Journal of Geophysical Research: Space Physics*, 121, 6889–6900. <https://doi.org/10.1002/2015JA022328>
- Kuhl, D. D., Rosmond, T. E., Bishop, C. H., McLay, J., & Baker, N. L. (2013). Comparison of hybrid ensemble/4DVar and 4DVar within the NAVDAS-AR data assimilation framework. *Monthly Weather Review*, 141(8), 2740–2758. <https://doi.org/10.1175/MWR-D-12-00182.1>

- Kurihara, J., Ogawa, Y., Oyama, S., Nozawa, S., Tsutsumi, M., Hall, C. M., & Fujii, R. (2010). Links between a stratospheric sudden warming and thermal structures and dynamics in the high-latitude mesosphere, lower thermosphere, and ionosphere. *Geophysical Research Letters*, 37, L13806. <https://doi.org/10.1029/2010GL043643>
- Laskar, F. I., McCormack, J. P., Chau, J. L., Pallamraju, D., Hoffmann, P., & Singh, R. P. (2019). Interhemispheric meridional circulation during sudden stratospheric warming. *Journal of Geophysical Research: Space Physics*, 124, 7112–7122. <https://doi.org/10.1029/2018JA026424>
- Li, N., Luan, X., Lei, J., Bolaji, O. S., Owolabi, C., Chen, J., & Ning, B. (2020). Variations of mesospheric neutral winds and tides observed by a meteor radar chain over China During the 2013 sudden stratospheric warming. *Journal of Geophysical Research: Space Physics*, 125, e2019JA027443. <https://doi.org/10.1029/2019JA027443>
- Limpasuvan, V., Orsolini, Y. J., Chandran, A., Garcia, R. R., & Smith, A. K. (2016). On the composite response of the MLT to major sudden stratospheric warming events with elevated stratopause. *Journal of Geophysical Research: Atmospheres*, 121, 4518–4537. <https://doi.org/10.1002/2015JD024401>
- Lindzen, R. S. (1981). Turbulence and stress owing to gravity wave and tidal breakdown. *Journal of Geophysical Research*, 86(C10), 9707–9714. <https://doi.org/10.1029/JC086iC10p09707>
- Liu, H. L. (2016). Variability and predictability of the space environment as related to lower atmosphere forcing. *Space Weather*, 14, 634–658. <https://doi.org/10.1002/2016SW001450>
- Liu, S. C., & Donahue, T. M. (1974a). The aeronomy of hydrogen in the atmosphere of the Earth. *Journal of the Atmospheric Sciences*, 31(4), 1118–1136. [https://doi.org/10.1175/1520-0469\(1974\)031<1118:TAOHIT>2.0.CO;2](https://doi.org/10.1175/1520-0469(1974)031<1118:TAOHIT>2.0.CO;2)
- Liu, S. C., & Donahue, T. M. (1974b). Mesospheric hydrogen related to exospheric escape mechanisms. *Journal of the Atmospheric Sciences*, 31(5), 1466–1470. [https://doi.org/10.1175/1520-0469\(1974\)031<1466:MHRTEE>2.0.CO;2](https://doi.org/10.1175/1520-0469(1974)031<1466:MHRTEE>2.0.CO;2)
- Liu, H., Doornbos, E., Yamamoto, M., & Tulasi Ram, S. (2011). Strong thermospheric cooling during the 2009 major stratosphere warming. *Geophysical Research Letters*, 38, L12102. <https://doi.org/10.1029/2011GL047898>
- Liu, H., Miyoshi, Y., Miyahara, S., Jin, H., Fujiwara, H., & Shinagawa, H. (2014). Thermal and dynamical changes of the zonal mean state of the thermosphere during the 2009 SSW: GAIA simulations. *Journal of Geophysical Research: Space Physics*, 119, 6784–6791. <https://doi.org/10.1002/2014JA020222>
- Liu, H. L., & Roble, R. G. (2002). A study of a self-generated stratospheric sudden warming and its mesospheric-lower thermospheric impacts using the coupled TIME-GCM/CCM3. *Journal of Geophysical Research*, 107(D23), 4695. <https://doi.org/10.1029/2001JD001533>
- Liu, X., Wang, W., Thayer, J. P., Burns, A., Sutton, E., Solomon, S. C., & Lucas, G. (2014). The winter helium bulge revisited. *Geophysical Research Letters*, 41, 6603–6609. <https://doi.org/10.1002/2014GL061471>
- Lukianova, R., Kozlovsky, A., Shalimov, S., Ulich, T., & Lester, M. (2015). Thermal and dynamical perturbations in the winter polar mesosphere-lower thermosphere region associated with sudden stratospheric warmings under conditions of low solar activity. *Journal of Geophysical Research: Space Physics*, 120, 5226–5240. <https://doi.org/10.1002/2015JA021269>
- MacDonald, G. J. F. (1963). The escape of helium from the Earth's atmosphere. *Reviews of Geophysics*, 1(3), 305–349. <https://doi.org/10.1029/RG001i003p00305>
- Manney, G. L., Schwartz, M. J., Krüger, K., Santee, M. L., Pawson, S., Lee, J. N., & Livesey, N. J. (2009). Aura Microwave Limb Sounder observations of dynamics and transport during the record-breaking 2009 Arctic stratospheric major warming. *Geophysical Research Letters*, 36, L12815. <https://doi.org/10.1029/2009GL038586>
- Matsuno, T. (1971). A dynamical model of the stratospheric sudden warming. *Journal of the Atmospheric Sciences*, 28, 1479–1494. [https://doi.org/10.1175/1520-0469\(1971\)028<1479:ADMOTS>2.0.CO;2](https://doi.org/10.1175/1520-0469(1971)028<1479:ADMOTS>2.0.CO;2)
- Matsuno, T., & Nakamura, K. (1979). The Eulerian-and Lagrangian-mean meridional circulations in the stratosphere at the time of a sudden warming. *Journal of the Atmospheric Sciences*, 36(4), 640–654. [https://doi.org/10.1175/1520-0469\(1979\)036<0640:TEALMM>2.0.CO;2](https://doi.org/10.1175/1520-0469(1979)036<0640:TEALMM>2.0.CO;2)
- Maute, A., Hagan, M. E., Yudin, V., Liu, H. L., & Yizengaw, E. (2015). Causes of the longitudinal differences in the equatorial vertical E × B drift during the 2013 SSW period as simulated by the TIME-GCM. *Journal of Geophysical Research: Space Physics*, 120, 5117–5136. <https://doi.org/10.1002/2015JA021126>
- McCormack, J., Hoppel, K., Kuhl, D., de Wit, R., Stober, G., Espy, P., et al. (2017). Comparison of mesospheric winds from a high-altitude meteorological analysis system and meteor radar observations during the boreal winters of 2009–2010 and 2012–2013. *Journal of Atmospheric and Solar-Terrestrial Physics*, 154, 132–166. <https://doi.org/10.1016/j.jastp.2016.12.007>
- McLandress, C., Scinocca, J. F., Shepherd, T. G., Reader, M. C., & Manney, G. L. (2013). Dynamical control of the mesosphere by orographic and nonorographic gravity wave drag during the extended northern winters of 2006 and 2009. *Journal of the Atmospheric Sciences*, 70(7), 2152–2169. <https://doi.org/10.1175/JAS-D-12-0297.1>
- Medvedeva, I., Semenov, A., Pogoreltsev, A., & Tatarnikov, A. (2019). Influence of sudden stratospheric warming on the mesosphere/lower thermosphere from the hydroxyl emission observations and numerical simulations. *Journal of Atmospheric and Solar-Terrestrial Physics*, 187, 22–32. <https://doi.org/10.1016/j.jastp.2019.02.005>
- Menk, F. W., Ables, S. T., Grew, R. S., Clilverd, M. A., & Sandel, B. R. (2012). The annual and longitudinal variations in plasmaspheric ion density. *Journal of Geophysical Research*, 117, A03215. <https://doi.org/10.1029/2011JA017071>
- Miyoshi, Y., Fujiwara, H., Jin, H., & Shinagawa, H. (2015). Impacts of sudden stratospheric warming on general circulation of the thermosphere. *Journal of Geophysical Research: Space Physics*, 120, 897–10,912. <https://doi.org/10.1002/2015JA021894>
- Mlynczak, M. G., Hunt, L. A., Marshall, B. T., Mertens, C. J., Marsh, D. R., Smith, A. K., & Gordley, L. L. (2014). Atomic hydrogen in the mesopause region derived from SABER: Algorithm theoretical basis, measurement uncertainty, and results. *Journal of Geophysical Research: Atmospheres*, 119, 3516–3526. <https://doi.org/10.1002/2013JD021263>
- Mlynczak, M. G., Hunt, L. A., Russell, J. M. III, & Marshall, B. T. (2018). Updated SABER night atomic oxygen and Implications for SABER ozone and atomic hydrogen. *Geophysical Research Letters*, 45, 5735–5741. <https://doi.org/10.1029/2018GL077377>
- Nath, O., Sridharan, S., & Gadhave, H. (2015). Equatorial stratospheric thermal structure and ozone variations during the sudden stratospheric warming of 2013. *Journal of Atmospheric and Solar-Terrestrial Physics*, 122, 129–137. <https://doi.org/10.1016/j.jastp.2014.11.003>
- Nicolet, M. (1961). Helium, an important constituent in the lower exosphere. *Journal of Geophysical Research*, 66(7), 2263–2264. <https://doi.org/10.1029/JZ066i007p02263>
- Oberheide, J., Forbes, J. M., Zhang, X., & Bruinsma, S. L. (2011). Climatology of upward propagating diurnal and semidiurnal tides in the thermosphere. *Journal of Geophysical Research*, 116, A11306. <https://doi.org/10.1029/2011JA016784>
- Oberheide, J., Pedatella, N. M., Gan, Q., Kumari, K., Burns, A. G., & Eastes, R. W. (2020). Thermospheric composition O/N₂ response to an altered meridional mean circulation during sudden stratospheric warmings observed by GOLD. *Geophysical Research Letters*, 47, e2019GL086313. <https://doi.org/10.1029/2019GL086313>

- Pedatella, N. M. (2016). Impact of the lower atmosphere on the ionosphere response to a geomagnetic superstorm. *Geophysical Research Letters*, 43(18), 9383–9389. <https://doi.org/10.1002/2016GL070592>
- Pedatella, N. M., & Forbes, J. M. (2010). Evidence for stratosphere sudden warming-ionosphere coupling due to vertically propagating tides. *Geophysical Research Letters*, 37, L11104. <https://doi.org/10.1029/2010GL043560>
- Pedatella, N. M., Richmond, A. D., Maute, A., & Liu, H. L. (2016). Impact of semidiurnal tidal variability during SSWs on the mean state of the ionosphere and thermosphere. *Journal of Geophysical Research: Space Physics*, 121, 8077–8088. <https://doi.org/10.1002/2016JA022910>
- Qian, L., Burns, A. G., Emery, B. A., Foster, B., Lu, G., Maute, A., et al. (2014). The NCAR TIE-GCM. In J. Huba, R. Schunk, G. Khazano (Eds.), *Modeling the ionosphere-thermosphere system, Geophysical Monograph Series* (Chap. 7). Washington, DC: American Geophysical Union. <https://doi.org/10.1002/9781118704417.ch7>
- Qian, L., Burns, A. G., Solomon, S. S., Smith, A. K., McNerney, J. M., Hunt, L. A., & Vitt, F. M. (2018). Temporal variability of atomic hydrogen from the mesopause to the upper thermosphere. *Journal of Geophysical Research: Space Physics*, 123, 1006–1017. <https://doi.org/10.1002/2017JA024998>
- Qian, L., Solomon, S. C., & Kane, T. J. (2009). Seasonal variation of thermospheric density and composition. *Journal of Geophysical Research*, 114, A01312. <https://doi.org/10.1029/2008JA013643>
- Reber, C. A., & Hays, P. B. (1973). Thermospheric wind effects on the distribution of helium and argon in the Earth's upper atmosphere. *Journal of Geophysical Research*, 78(16), 2977–2991. <https://doi.org/10.1029/JA078i016p02977>
- Rezac, L., Kutepov, A., Russell, J., Feofilov, A., Yue, J., & Goldberg, R. (2015). Simultaneous retrieval of $T(p)$ and CO_2 VMR from two-channel non-LTE limb radiances and application to daytime SABER/TIMED measurements. *Journal of Atmospheric and Solar-Terrestrial Physics*, 130–131, 23–42. <https://doi.org/10.1016/j.jastp.2015.05.004>
- Richards, P. G., Fennelly, J. A., & Torr, D. G. (1994). EUVAC: A solar EUV flux model for aeronomic calculations. *Journal of Geophysical Research*, 99(A5), 8981–8992. <https://doi.org/10.1029/94JA00518>
- Richmond, A. D., Ridley, E. C., & Roble, R. G. (1992). A thermosphere/ionosphere general circulation model with coupled electrodynamics. *Geophysical Research Letters*, 19(6), 601–604. <https://doi.org/10.1029/92GL00401>
- Roble, R. G., & Ridley, E. (1987). An auroral model for the NCAR thermospheric general circulation model (TGCM). *Annales Geophysicae*, 5A, 369–382. Retrieved from <http://n2t.net/ark:/85065/d70v8ckz>
- Roble, R. G., & Ridley, E. C. (1994). A thermosphere-ionosphere-mesosphere-electrodynamics general circulation model (time-GCM): Equinox solar cycle minimum simulations (30–500 km). *Geophysical Research Letters*, 21(6), 417–420. <https://doi.org/10.1029/93GL03391>
- Siddiqui, T. A., Maute, A., & Pedatella, N. M. (2019). On the importance of interactive ozone chemistry in earth-system models for studying mesosphere-lower thermosphere tidal changes during sudden stratospheric warmings. *Journal of Geophysical Research: Space Physics*, 124, 10,690–10,707. <https://doi.org/10.1029/2019JA027193>
- Siskind, D. E., Coy, L., & Espy, P. (2005). Observations of stratospheric warmings and mesospheric coolings by the TIMED SABER instrument. *Geophysical Research Letters*, 32, L09804. <https://doi.org/10.1029/2005GL022399>
- Siskind, D. E., Drob, D. P., Dymond, K. F., & McCormack, J. P. (2014). Simulations of the effects of vertical transport on the thermosphere and ionosphere using two coupled models. *Journal of Geophysical Research: Space Physics*, 119, 1172–1185. <https://doi.org/10.1002/2013JA019116>
- Siskind, D. E., Eckermann, S. D., McCormack, J. P., Coy, L., Hoppel, K. W., & Baker, N. L. (2010). Case studies of the mesospheric response to recent minor, major, and extended stratospheric warmings. *Journal of Geophysical Research*, 115, D00N03. <https://doi.org/10.1029/2010JD014114>
- Siskind, D. E., Jones, M. Jr., Drob, D. P., McCormack, J. P., Hervig, M. E., Marsh, D. R., & Mitchell, N. J. (2019). On the relative roles of dynamics and chemistry governing the abundance and diurnal variation of low-latitude thermospheric nitric oxide. *Annales Geophysicae*, 37(1), 37–48. <https://doi.org/10.5194/angeo-37-37-2019>
- Siskind, D. E., Merkel, A. W., Marsh, D. R., Randall, C. E., Hervig, M. E., Mlynarczyk, M. G., & Russell, J. M. III (2018). Understanding the effects of polar mesospheric clouds on the environment of the upper mesosphere and lower thermosphere. *Journal of Geophysical Research: Atmospheres*, 123, 11,705–11,719. <https://doi.org/10.1029/2018JD028830>
- Smith, A. K., Harvey, V. L., Mlynarczyk, M. G., Funke, B., Garc a-Comas, M., Hervig, M., et al. (2013). Satellite observations of ozone in the upper mesosphere. *Journal of Geophysical Research: Atmospheres*, 118, 5803–5821. <https://doi.org/10.1002/jgrd.50445>
- Solomon, S. C., & Qian, L. (2005). Solar extreme-ultraviolet irradiance for general circulation models. *Journal of Geophysical Research*, 110, A10306. <https://doi.org/10.1029/2005JA011160>
- Stauffer, D. R., & Seaman, N. L. (1990). Use of four-dimensional data assimilation in a limited-area mesoscale model. Part I: Experiments with synoptic-scale data. *Monthly Weather Review*, 118(6), 1250–1277. [https://doi.org/10.1175/1520-0493\(1990\)118<1250:UOFDDA>2.0.CO;2](https://doi.org/10.1175/1520-0493(1990)118<1250:UOFDDA>2.0.CO;2)
- Stauffer, D. R., & Seaman, N. L. (1994). Multiscale four-dimensional data assimilation. *Journal of Applied Meteorology*, 33(3), 416–434. [https://doi.org/10.1175/1520-0450\(1994\)033<0416:MFDFA>2.0.CO;2](https://doi.org/10.1175/1520-0450(1994)033<0416:MFDFA>2.0.CO;2)
- Stober, G., Baumgarten, K., McCormack, J. P., Brown, P., & Czarniecki, J. (2019). Comparative study between ground-based observations and NAVGEM-HA reanalysis data in the MLT region. *Atmospheric Chemistry and Physics Discussions*, 2019, 1–37. <https://doi.org/10.5194/acp-2019-1006>
- Stober, G., Jacobi, C., Matthias, V., Hoffmann, P., & Gerding, M. (2012). Neutral air density variations during strong planetary wave activity in the mesopause region derived from meteor radar observations. *Journal of Atmospheric and Solar-Terrestrial Physics*, 74, 55–63. <https://doi.org/10.1016/j.jastp.2011.10.007>
- Sutton, E. K. (2016). Interhemispheric transport of light neutral species in the thermosphere. *Geophysical Research Letters*, 43, 12,325–12,332. <https://doi.org/10.1002/2016GL071679>
- Swadley, S. D., Poe, G. A., Bell, W., Hong, Y., Kunee, D. B., McDermid, I. S., & Leblanc, T. (2008). Analysis and characterization of the SSMIS upper atmosphere sounding channel measurements. *IEEE Transactions on Geoscience and Remote Sensing*, 46(4), 962–983. <https://doi.org/10.1109/TGRS.2008.916980>
- Wang, J. C., Chang, L. C., Yue, J., Wang, W., & Siskind, D. E. (2017). The quasi 2 day wave response in TIME-GCM nudged with NOGAPS-ALPHA. *Journal of Geophysical Research: Space Physics*, 122, 5709–5732. <https://doi.org/10.1002/2016JA023745>
- Woods, T. N., & Rottman, G. J. (2002). Solar ultraviolet variability over time periods of aeronomic interest. In M. Mendillo, A. Nagy, J. H. Waite (Eds.), *Atmospheres in the Solar System: Comparative Aeronomy, Geophysical Monograph Series* (Vol. 130, pp. 221–233). Washington, DC: American Geophysical Union. <https://doi.org/10.1029/130GM14>
- Yamashita, C., Liu, H. L., & Chu, X. (2010). Responses of mesosphere and lower thermosphere temperatures to gravity wave forcing during stratospheric sudden warming. *Geophysical Research Letters*, 37, L09803. <https://doi.org/10.1029/2009GL042351>

- Yamazaki, Y., Kosch, M. J., & Emmert, J. T. (2015). Evidence for stratospheric sudden warming effects on the upper thermosphere derived from satellite orbital decay data during 1967–2013. *Geophysical Research Letters*, 42, 6180–6188. <https://doi.org/10.1002/2015GL065395>
- Yamazaki, Y., & Richmond, A. D. (2013). A theory of ionospheric response to upward-propagating tides: Electrodynamical effects and tidal mixing effects. *Journal of Geophysical Research: Space Physics*, 118, 5891–5905. <https://doi.org/10.1002/jgra.50487>
- Yan, X., Wright, J. S., Zheng, X., Livesey, N. J., Vömel, H., & Zhou, X. (2016). Validation of Aura MLS retrievals of temperature, water vapour and ozone in the upper troposphere and lower-middle stratosphere over the Tibetan Plateau during boreal summer. *Atmospheric Measurement Techniques*, 9(8), 3547–3566. <https://doi.org/10.5194/amt-9-3547-2016>
- Yigit, E., & Medvedev, A. S. (2012). Gravity waves in the thermosphere during a sudden stratospheric warming. *Geophysical Research Letters*, 39, L21101. <https://doi.org/10.1029/2012GL053812>
- Yigit, E., & Medvedev, A. S. (2016). Role of gravity waves in vertical coupling during sudden stratospheric warmings. *Geoscience Letters*, 3(1), 27. <https://doi.org/10.1186/s40562-016-0056-1>
- Yue, J., Jian, Y., Wang, W., Meier, R., Burns, A., Qian, L., & Mlynarczyk, M. (2019). Annual and semiannual oscillations of thermospheric composition in TIMED/GUVI limb measurements. *Journal of Geophysical Research: Space Physics*, 124, 3067–3082. <https://doi.org/10.1029/2019JA026544>
- Yue, X., Schreiner, W. S., Lei, J., Rocken, C., Hunt, D. C., Kuo, Y. H., & Wan, W. (2010). Global ionospheric response observed by COSMIC satellites during the January 2009 stratospheric sudden warming event. *Journal of Geophysical Research*, 115, A00G09. <https://doi.org/10.1029/2010JA015466>
- Zülicke, C., & Becker, E. (2013). The structure of the mesosphere during sudden stratospheric warmings in a global circulation model. *Journal of Geophysical Research: Atmospheres*, 118, 2255–2271. <https://doi.org/10.1002/jgrd.50219>
- Zülicke, C., Becker, E., Matthias, V., Peters, D. H. W., Schmidt, H., Liu, H. L., & Mitchell, D. M. (2018). Coupling of stratospheric warmings with mesospheric coolings in observations and simulations. *Journal of Climate*, 31(3), 1107–1133. <https://doi.org/10.1175/JCLI-D-17-0047.1>